Building and Environment 264 (2024) 111919

Contents lists available at ScienceDirect

Building and Environment

journal homepage: www.elsevier.com/locate/buildenv

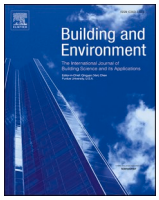

Pollutant cross-transmission in courtyard buildings: Wind tunnel experiments and computational fluid dynamics (CFD) evaluation

Hao Sun [a,*], John S. Owen [b], Salah Almazmumi [a,c], Chong Liu [d], Murtaza Mohammadi [a], Abdullah Dik [a,e], Carlos Jimenez-Bescos [f], John Kaiser Calautit [a,**]

[a] Department of Architecture and Built Environment, University of Nottingham, UK
[b] Department of Civil Engineering, University of Nottingham, UK
[c] Architectural Engineering Department, Najran University, 66462, Najran, Saudi Arabia
[d] Department of Civil and Environmental Engineering, Imperial College London, UK
[e] Faculty of Engineering, Iskenderun Technical University, Hatay, Turkey
[f] Westminster Business School, University of Westminster, UK

ARTICLE INFO

Keywords:
Courtyard building
Indoor-outdoor pollutant cross-transmission
Air quality
Wind tunnel experiments
Computational fluid dynamics (CFD)

ABSTRACT

Courtyards, a historical architectural feature surrounded by buildings, are common in urban housing and residential complexes. These spaces, often open-air and with rooms facing them, are crucial for daylight and natural ventilation. While courtyards are essential for introducing fresh airflow into adjacent indoor areas, the effectiveness of natural ventilation may be compromised due to potentially poor air circulation from limited openings. This raises a significant concern: could the design of courtyards inadvertently facilitate pollutant cross-transmission? Despite a wealth of research focused on airflow within courtyards, the indoor spaces in proximity to these courtyards have often been neglected in previous works, particularly concerning the exchange of pollutants between the indoor and courtyard environment. This research investigates the dynamics of indoor-outdoor pollutant cross-transmission in courtyard buildings, assessing factors like external wind flow patterns and internal pollutant sources. Wind tunnel experiments were conducted to measure internal pressure and CO_2 concentration and to validate a computational model of the courtyard with 12 rooms. The validated Computational Fluid Dynamics (CFD) models were used to simulate the dispersion of pollutants from internal rooms under different wind conditions. The results showed that the k-epsilon Realizable model accurately simulated internal surface pressure distribution and pollutant dispersion in the courtyard building. It was observed that when pollutants were released from the downwind east-facing ground floor room, CO_2 concentrations in adjacent side rooms on the same floor were significantly higher, increasing from the baseline of 400 ppm and reaching up to 3211 ppm in the north-facing room at a wind speed of 4.51 m/s and wind direction of 0°. Conversely, when pollutants originated from north- and south-facing side rooms, pollutants were minimally dispersed to adjacent rooms. Furthermore, at a wind direction of 45°, pollutants from wind-exposed rooms predominantly dispersed to downwind rooms, with peak concentrations exceeding 2400 ppm in downwind rooms. These findings demonstrate that pollutant dispersion is highly dependent on wind direction and the location of the pollutant source. The study concludes that while courtyards enhance indoor environmental quality through natural ventilation, their design must be carefully considered to prevent unintended pollutant cross-transmission, particularly under varying wind conditions and pollutant source locations.

* Corresponding author.
** Corresponding author.
E-mail addresses: Hao.Sun@nottingham.ac.uk (H. Sun), John.Calautit1@nottingham.ac.uk (J.K. Calautit).

https://doi.org/10.1016/j.buildenv.2024.111919
Received 5 April 2024; Received in revised form 23 July 2024; Accepted 4 August 2024
Available online 6 August 2024

1. Introduction and literature review

1.1. Background and motivation

Courtyards serve as vital social spaces, fostering community interactions and enhancing urban environments [1,2]. Beyond their social benefits, they are also recognized for facilitating natural light, promoting natural ventilation, and providing passive cooling within dwellings [3]. However, the aspect of pollutant accumulation and dispersion within these spaces remains underexplored [4]. Courtyard buildings, through their unique structural design, create distinct airflow patterns [5–8] that can inadvertently transport indoor pollutants across rooms via the courtyard.

In considering the dynamic relationship between architectural form and environmental flow in these semi-enclosed spaces, it becomes apparent that courtyards play a more active role than previously understood. Unlike isolated structures, the design of courtyards creates a unique microclimate. Here, air movement is primarily dictated by the courtyard's geometry rather than merely reacting to external wind conditions [9]. This complex interaction between architecture and airflow is often underappreciated, yet crucial in understanding how it may amplify or mitigate pollutant levels in these environments.

To contextualize the discussion, consider a practical scenario: an individual cooking on the upwind side of a courtyard building. The process not only releases culinary aromas but also potentially hazardous cooking emissions. These are not confined to the immediate vicinity; rather, they are likely to be carried across the courtyard by prevailing winds, infiltrating neighboring living spaces (see Fig. 1). This situation leads us to ask some important questions: When it comes to the design of courtyards, which side — the sides sheltered from the wind (downwind), or the sides exposed to it (upwind)—is less likely to facilitate the transfer of pollutants from one unit to another through the courtyard? And conversely, which side is more prone to unintentional pollutant exchange? Additionally, how does the height of rooms within the courtyard affect the dispersion of pollutants? Which floors are most impacted by such pollutant transfer? Gaining insight into the answers to these questions is crucial for resolving the complexities of how pollutants disperse within architectural layouts like courtyards. Furthermore, this understanding can guide design strategies aimed at reducing the health risks that can inadvertently arise from an architectural style intended to improve urban living conditions.

1.2. Literature review

Considerable research has been conducted on various aspects of microclimates within courtyards. Previous works have discussed the influence of geometry, orientation, wall materials, and landscape elements such as ponds, trees, and grass on courtyard microclimates [10–16]. Courtyard buildings, with their unique airflow characteristics that differ from various other architectural forms, potentially create a stack effect in courtyards depending on specific indoor-outdoor conditions. This phenomenon is driven by temperature differences between the interior and exterior [6]. This architectural feature imparts a distinctive capability for passive microclimate regulation, allowing courtyard structures to adeptly adjust and harmonize with their surrounding environment.

Recent studies have shown the significant role of courtyard design in enhancing air quality and managing pollutant levels. Specifically, these studies emphasize how the geometry and orientation of courtyards impact the internal airflow dynamics and discuss the effects of these design elements on air quality and pollutant concentrations within courtyard architecture. The investigations by Ref. [4] assessed the implications of courtyard design on disease transmission. Their simulations underscored that well-designed courtyards can effectively reduce the risk of respiratory infections by enhancing airflow and diluting concentrations of airborne pollutants. Similarly, the work by Ref. [17] explored the effects of courtyard design on airflow and pollutant dispersion. Their findings underscore the critical function of courtyard configurations, especially central and internal courtyards, in mitigating pollutant concentrations at pedestrian levels. Simulations of various architectural layouts revealed how courtyard spaces can influence pollutant dispersion by modifying airflow. While these studies mainly address the impact of courtyard design on air quality and pollutant movement, emphasizing how courtyard shape affects respiratory infections and pollution at pedestrian levels, the present study focuses on the specific issue of pollutants re-entering through the courtyard. This aspect is vital for enhancing courtyard architecture to improve air quality and health outcomes.

You et al. [18] demonstrated the impact of courtyard shape and elevation on the vertical and horizontal dispersion of cooking-related

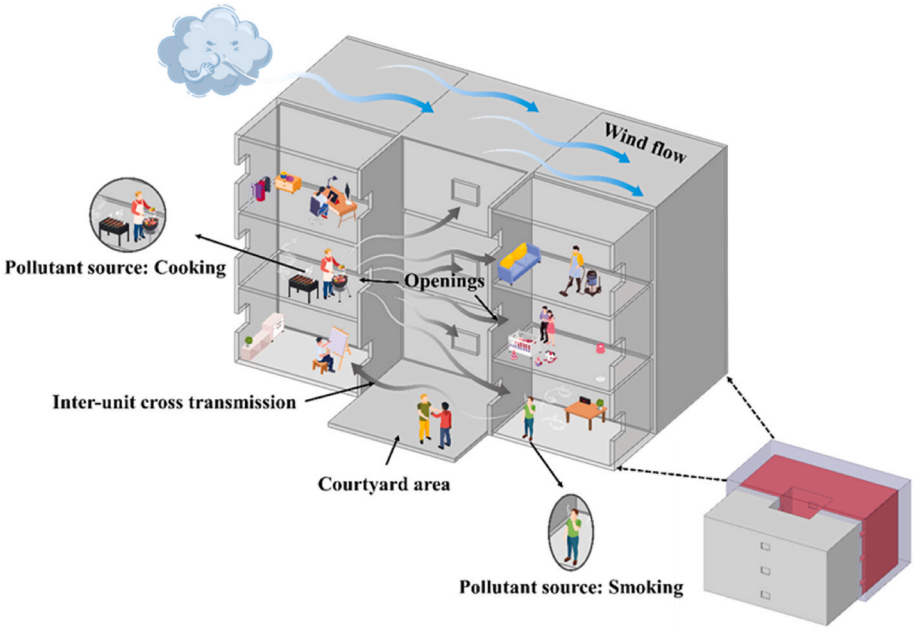

Fig. 1. Cross-transmission of pollutants between naturally ventilated courtyard units.

pollutants within high-rise residential buildings. Their simulations suggested that certain courtyard designs facilitate the upward movement of pollutants and thereby lower contamination. This insight is invaluable to our study as it provides information on the optimization of air movement and pollutant control through courtyard design. Lozhkin et al. [19] conducted a detailed analysis of pollution issues caused by vehicular exhaust in the enclosed courtyards of St. Petersburg, indicating significantly higher concentrations of pollutants in enclosed courtyards compared to their open counterparts, particularly on days with low wind speeds. These results highlight that it is essential to consider ventilation and pollutant dispersion in courtyard design, acknowledging potential pollutant accumulation even in open courtyards. Nosek et al. [20] further corroborated the influence of courtyard architecture on street canyon ventilation through wind tunnel experimental simulations. Their studies indicated that courtyards, particularly those with pitched roofs, can significantly enhance ventilation effectiveness within urban canyons, directly affecting pollutant distribution and cross-transmission within the courtyard. Moonen et al. [21] employed CFD to assess the ventilation potential of courtyards and urban canyons, with a particular emphasis on wind orientation and flow angles. Their research, using both Reynolds-Averaged Navier-Stokes (RANS) and Large Eddy Simulation (LES) methodologies, outlined the important role of courtyard dimensions and geometry as a facilitator for air renewal and pollutant dispersion. The systematic investigation encompassed various urban block types.

1.3. Research gaps and novelty

Previous studies have primarily focused on the aerothermal environment, comfort, and the impact on urban microclimates of courtyard architecture, showing limitations in exploring the relationship between courtyard structures and pollutant dispersion. These studies tend to emphasize the inherent features of courtyards, such as geometric structure and orientation, and their impact on airflow dynamics and air quality. Although they discuss the relationship of pollutant dispersion, cross-ventilation, and accumulation within courtyards, they often overlook the significant impact of the courtyards' unique enclosed or semi-enclosed nature and their connectivity with surrounding buildings on pollutant dispersion. Simultaneously, these studies have not fully explored complex mechanisms of inter-unit pollutant transmission.

Moreover, in the context of pollution dispersion in the courtyard, integrating wind tunnel experiments and CFD simulations is rarely employed to study these complex phenomena. Existing research usually focuses on pollutant dispersion near an isolated cubic building [22–26] or urban blocks [27–31]. Studies on indoor and outdoor pollutant distribution also primarily concentrate on external pollution, particularly how pollution near street canyons affects indoor air quality [32–38]. Research on the movement, dispersion, and distribution of pollutants inside and outside enclosed courtyard buildings is still in its early stages, especially lacking studies on the pathways of pollutants spreading from within courtyard structures to the outside and back indoors.

1.4. Aim and objectives

The aim of the current study is to evaluate the design of courtyard buildings to reduce the spread of pollutants and enhance the overall environmental health standards within urban living spaces. Our study addresses the shortcomings in the literature by investigating the dynamics of wind-driven pollutant dispersion in courtyard buildings through a combination of wind tunnel experiments and CFD simulations. This is achieved by meeting the following research objectives.

1. Validate the results obtained from ANSYS Fluent CFD simulations using wind tunnel experiments data. This validation process is critical to ensure the findings are reliable and applicable across various scenarios.
2. Integrate wind tunnel experiments with CFD analyses. The use of complementary techniques offers richer insights, focusing on how different wind directions and speeds influence the dispersion of pollutants within courtyard architectures. Understanding these dynamics is crucial for accurately assessing the impact of environmental conditions on air quality in these spaces.
3. Examine the effects of varying external conditions, such as wind direction and speed, on the movement and concentration of pollutants within courtyards. This understanding is essential for predicting and managing air quality in urban living environments.
4. Analyze the impact of pollutant source locations. Investigating how the location of pollutant sources within the courtyard affects dispersion patterns and concentration levels of pollutants like CO_2 will provide deeper insights into the spatial dynamics of air quality within these enclosed spaces.
5. Evaluate optimal and adverse scenarios that improve natural ventilation and pollutant removal in courtyards, thereby enhancing indoor air quality.

This study employs an idealized model to simulate the courtyard geometry and environmental conditions. While the model provides a controlled framework to investigate pollutant dispersion, it does not encompass all real-world complexities, such as simultaneous pollutant-generating activities. Nevertheless, this analysis emphasizes the complex dynamics of pollutant dispersion in courtyard buildings and highlights the necessity of such studies for practical applications.

The paper is set out as follows. Section 1 provides the context for the study and establishes the aim and objectives. Section 2 describes the wind tunnel experiment, while Section 3 presents the CFD approaches, including the evaluation of different turbulence models, a mesh refinement study, and validation of the selected model. Section 4 presents the numerical simulation outcomes for diverse pollutant sources under varying wind speeds and directions. Finally, Sections 5 and 6 discuss the study's results and limitations, provide a conclusion, and outline potential future work.

2. Experimental method

2.1. Physical model and wind tunnel experimental setup

The experimental study employed a courtyard model at a 1:50 scale. This model was constructed from acrylic panels with a thickness of 3 mm. As presented in Fig. 2 (b), the dimensions were 300 mm × 300 mm x 180 mm (L x W x H). The model comprises 4 three-story buildings that face the courtyard, each measuring 100 mm × 100 mm x 60 mm. These buildings are interconnected by walls, creating a closed courtyard structure. Each courtyard-facing room within these buildings features two windows measuring 20 mm × 15 mm to facilitate crossflow ventilation, as shown in Fig. 2 (c) and 2 (d).

As depicted in Fig. 2 (a), the experiments were conducted in the atmospheric boundary layer (ABL) wind tunnel laboratory within the Department of Civil Engineering at the University of Nottingham. The test section of this wind tunnel has dimensions of 3.1 m in length, 2.4 m in width, and 1.9 m in height. Preceding the 2 m diameter circular turntable is an 11.5 m long fetch. The wind direction can be modified by rotating this turntable. Given the dimensions of the 1:50 model and the wind tunnel section, the blockage ratio attributed to the scaled-down courtyard model in the wind tunnel is 1.18 %. No adjustments were made to the measurements derived from these configurations, as recommended by Mercker [39].

In our wind tunnel experiments, similarity criteria are essential to ensure that our scaled model accurately represents full scale conditions, particularly fluid dynamics. A key aspect of these criteria is the establishment of dynamic similarity. In this study, we did not match the Reynolds number because of the wind tunnel speed limitations, although we did exceed the threshold highlighted by previous works.

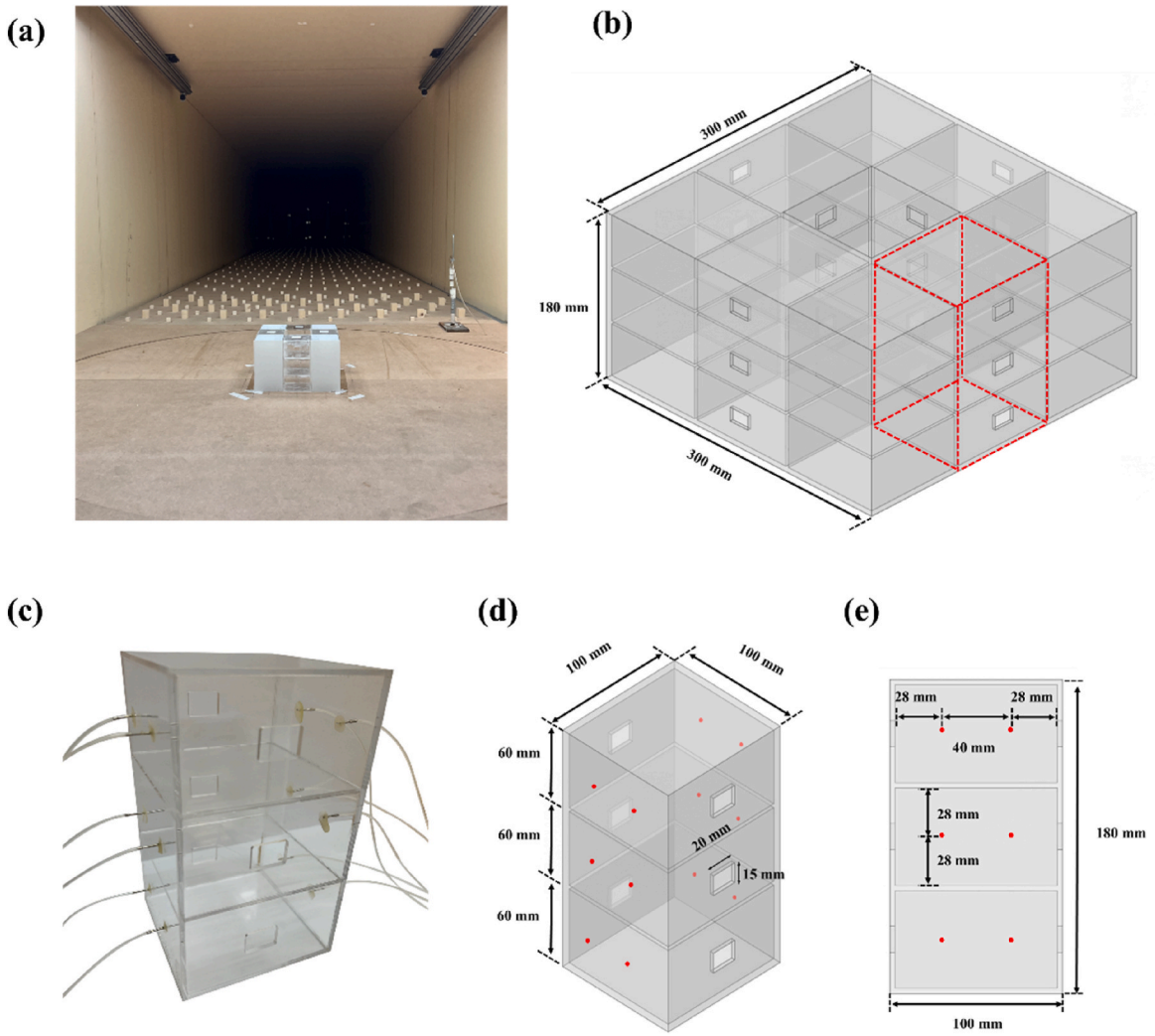

Fig. 2. (a) The courtyard model positioned on the turntable within the ABL wind tunnel. (b) Overall dimensions of the courtyard building model. (c) Single building model and connection of pressure tubes. (d) Dimensions of a single building and windows. (e) Arrangement of pressure measurement points on the side wall within the indoor domain.

For our experiments, reference wind speeds were measured at the height of the building. Two different values were used: $U_{ref} = 4.51$ m/s and $U_{ref} = 8.86$ m/s. At these speeds, the Reynolds numbers calculated using a characteristic length (the height of the courtyard model) of 180 mm were 5.49×10^4 and 1.08×10^5, respectively. These values exceeded the threshold (Reynolds number $= 3.3 \times 10^4$) indicated by Ref. [40] for achieving Reynolds number independence in similar studies.

This independence from the Reynolds number suggests that the flow characteristics around the model are comparable to those in the actual environment, thus satisfying the criteria for dynamic similarity. Cui et al. [41] highlighted the importance of Reynolds number independence in indoor flow and pollutant dispersion studies. This research supports our approach by showing that flow characteristics remain consistent within a specific Reynolds number range, confirming our model's reliability. By achieving and verifying these Reynolds numbers, our model under both wind conditions accurately represents full-scale scenarios, adhering to the essential similarity criteria for modeling and analysis.

An ABL velocity profile was established utilizing a combination of spires and surface roughness elements. Average velocity and turbulence intensity were precisely measured using the Testo 450i thermal anemometer. The instrument has a measuring range from 0 to 30 m/s, a high-resolution capability of 0.01 m/s, and an accuracy of ± (0.1 m/s + 5 % of mv) for speeds up to 2 m/s and ± (0.3 m/s + 5 % of mv) for

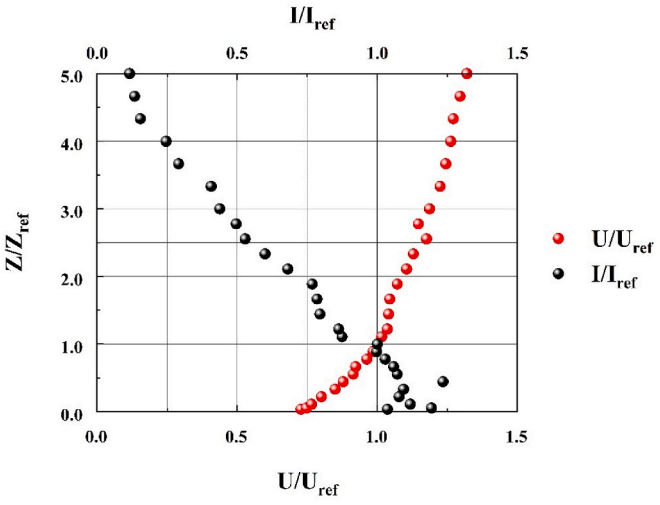

Fig. 3. Measured average velocity and turbulence intensity of wind profile.

speeds up to 15 m/s. The profiles of inlet velocity and turbulence intensity at the centre of the turntable in the absence of the building models are shown in Fig. 3 respectively.

2.2. Wind tunnel experimental setup for the pressure measurement

To assess the pressure distribution within the courtyard building, 2 pressure taps were located inside each of the rooms, as illustrated in Fig. 2 (e). In total, 48 pressure taps were employed to measure the indoor pressure coefficients. Pressure taps were connected to a 64 channel Scanivalve MPS4264 digital pressure transducer using vinyl tubing with an external diameter of 0.001 m and a length of 1.2 m. The digital sensor array has a full-scale measurement range of 995.4 Pa with an accuracy of ±0.06 % FS. The backing pressure was taken from the static port of a Pitot-static tube positioned at the reference height of 180 mm in line with the front of the model. The Pitot-static tube was also used to measure the mean wind speed. Pressure data were collected for 200 s at a sampling rate of 50 Hz.

2.3. Wind tunnel experimental setup for the CO_2 measurement

The study also included CO_2 measurements for four test scenarios: the model oriented at 0° with wind speed of $U_{ref} = 4.51$ m/s and $U_{ref} = 8.86$ m/s, and the model positioned at 45° with wind speeds set at $U_{ref} = 4.51$ m/s and $U_{ref} = 8.86$ m/s.

To simulate the dispersion of an indoor source of gaseous pollutants,

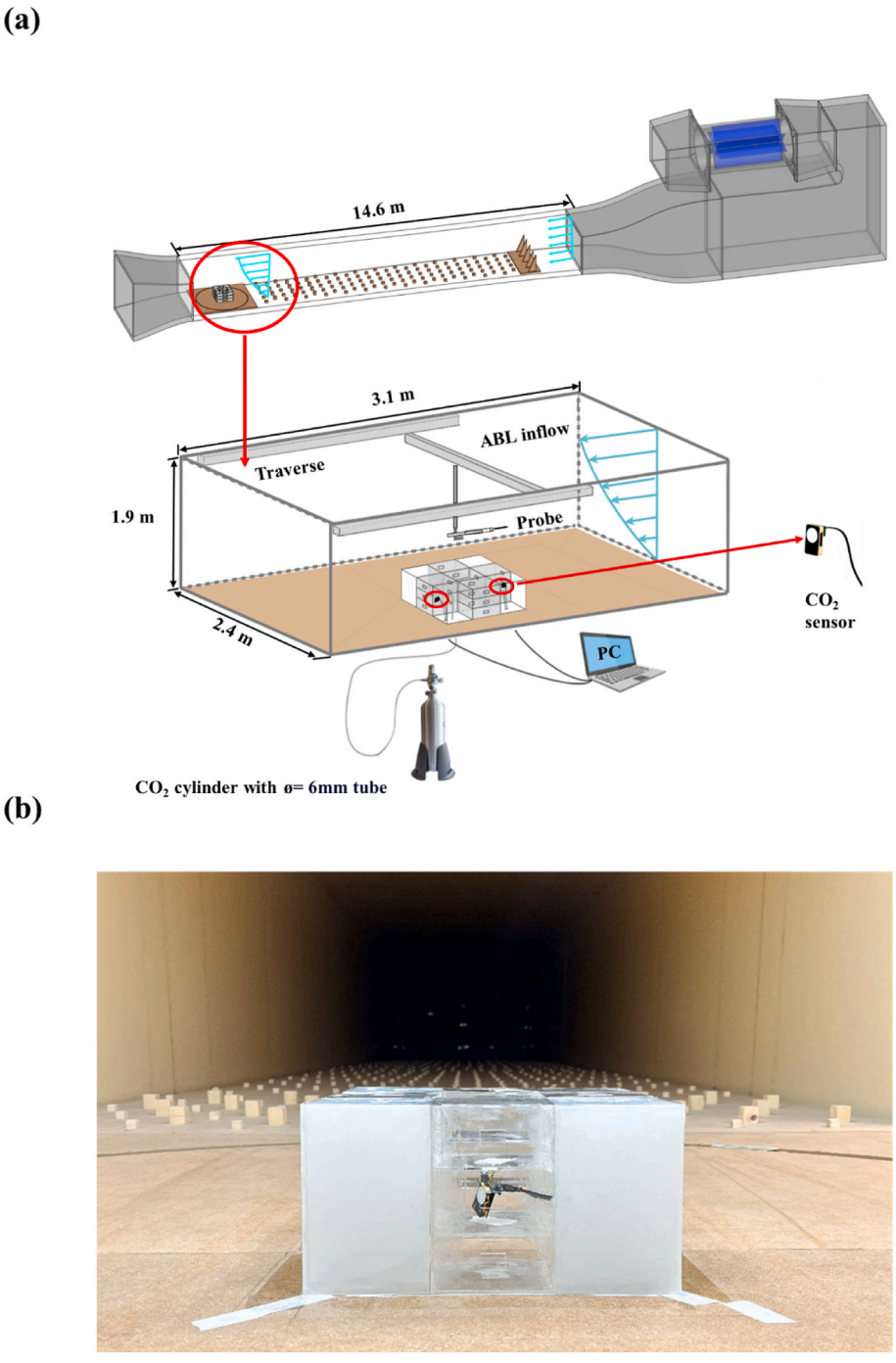

Fig. 4. (a) Wind tunnel CO_2 dispersion measurement setup. (b) The courtyard model with CO_2 sensors in the wind tunnel.

the tracer gas CO_2 was released from the CO_2 cylinder. As shown in Fig. 4 (a) and 4 (b), CO_2 concentration sensors were placed on the second floor of both the upwind and downwind sides of the model building. The CozIR®-LP CO_2 sensor, which employs NDIR solid-state LED optics and has a measurement precision of 30 ppm, was employed to measure the CO_2 concentration. These sensors can monitor CO_2 concentrations up to 5000 ppm and feature an automatic calibration mechanism. A polyurethane tube, 6 mm in outer diameter, was positioned on the same floor of the upwind building, and it was connected to a 1 L aluminum CO_2 cylinder under the wind tunnel. This cylinder was equipped with a control valve to ensure a consistent release of CO_2.

Throughout the experiment, varying CO_2 emission rates were established based on wind speeds and model orientations to guarantee accurate readings by both sensors while ensuring that the CO_2 concentration did not exceed the sensor's maximum limit of 5000 ppm. Specifically, with the model at 0°, a steady release rate of 2.8 ml/s was maintained for U_{ref} = 4.51 m/s and U_{ref} = 8.86 m/s wind speeds. Conversely, when the model was at 45°, the release rates were set at 0.45 ml/s and 0.8 ml/s for wind speeds of U_{ref} = 4.51 m/s and U_{ref} = 8.86 m/s, respectively. This adjustment was necessary because, at a 45° wind angle, the transmission of pollutants across rooms caused CO_2 levels in the source room (RWF) to approach the sensor's maximum capacity of 5000 ppm. Therefore, the emission rates were reduced through careful calibration to maintain accurate and reliable readings. Following sensor calibration, a consistent CO_2 release was initiated, and data recording ceased once readings from both sensors stabilized.

It should be noted that the experimental setup utilized an idealized model of courtyard buildings with simplified geometry and uniform window sizes to focus on the fundamental aspects of pollutant dispersion. This approach does not account for all real-world complexities, such as simultaneous pollutant-generating activities or the impact of surrounding buildings. These simplifications were necessary to isolate specific variables and control the experimental conditions.

3. CFD method

3.1. Numerical methods and solver settings

This research employs the control volume method, using the software ANSYS Fluent 18.1, to conduct steady-state RANS calculations for flow and mass fraction equations. 3D CFD simulations were run, assuming a fully turbulent and incompressible flow. The RANS equations are solved using the *k*-epsilon Realizable model. The employed CFD program adopts the Finite Volume Method (FVM) with a semi-implicit velocity-pressure coupling algorithm (SIMPLE) for the second-order upwind discrete pressure correlation equations. Solution convergence is established when the typical convergence thresholds are established at 10^{-4}, for U_x, U_y, U_z reaching 10^{-6}, and for *k* and epsilon set at 10^{-4} and 10^{-5}, respectively. For the concentration variable, the threshold was set at 10^{-7}.

This study also evaluates the predictive capabilities of three turbulence models: the *k*-epsilon standard model [42], the *k*-epsilon RNG model [43], and the *k*-epsilon Realizable model [44] for pressure distribution and CO_2 dispersion in wind tunnels. Based on the results (refer to Figs. 7 and 8), the *k*-epsilon Realizable model was chosen for further in-depth analysis. The turbulent Schmidt number (S_{ct}) is vital in dispersion simulation. For all cases, an S_{ct} value of 0.7 was adopted. Tominaga et al. [45] found this value to align well with experimental results when comparing experiments and simulations for air pollution dispersion around a building. This selection is further supported by Ref. [46], based on the comparison between wind tunnel and CFD results. The species transport equations and *k*-epsilon Realizable equations employed in this study are unchanged and fully detailed in Ref. [47].

3.2. Courtyard geometry, computational domain, and boundary conditions

As demonstrated in Fig. 5 (a), for both modeling and wind tunnel experiments, the dimensions of the courtyard building model and the computational fluid domain were replicated at a 1:1 scale. The model's dimensions are 300 mm × 300 mm x 180 mm. Each floor comprises four test rooms in the east, west, north, and south corners. Rooms adjacent to the courtyard were distinctly labeled based on floor and orientation to facilitate the analysis across different rooms, as presented in Fig. 5 (b). Fig. 5 (c) illustrates nine sampling points strategically positioned at the mid-height of each test room, ensuring uniform distribution for the collection of CO_2 concentration data. Fig. 5 (d) shows the fluid domain's dimensions, which mirror those of the test section, measuring 2.4 m × 1.9 m x 3.1 m.

In the computational domain, both side and top walls were designated as symmetry walls. The spacing between the courtyard and the two side symmetry walls was set at 1050 mm, while the distances from the courtyard to the velocity inlet and pressure outlet were 950 mm and 1850 mm, respectively. The distance between the courtyard and the domain's top wall was 1882 mm. In all CFD simulation scenarios, the pollutant source is modeled as a cylindrical volume. The cylinder has a 6 mm diameter cross-section and a height of 1 mm, with the top face set as a carbon dioxide inlet. The source is positioned 20 mm above the floor (as shown in Fig. A.1), and the release rate of CO_2 is consistently set at 2.8 ml/s. For both the inlet and outlet, the initial configurations are maintained with a CO_2 concentration of 400 ppm and a temperature of 300K.

The inlet wind profile was consistent for all simulation scenarios. The average wind speed was derived using the power law formula given by:

$$u(z) = u_{ref}\left(\frac{z}{z_{ref}}\right)^{\alpha} \quad (1)$$

where $u(z)$ is the mean velocity at height z (m/s), $\alpha = 0.145$, which is the power law exponent found by curve fitting the wind tunnel data, z_{ref} = 180 mm is the reference height corresponding to the height of the courtyard model, and u_{ref} is the reference velocity at height z_{ref}, which are 4.51 m/s and 8.86 m/s. Given these velocities, the Reynolds numbers were calculated to be approximately 5.49×10^4 and 1.08×10^5, respectively.

3.3. Grid and sensitivity analysis

The accuracy of the numerical simulation and computation time are influenced by the quality of the mesh used in modeling. The mesh for the fluid domain was generated as a tetrahedral mesh in ANSYS Meshing. Near the courtyard building's walls, windows, and floors, a finer grid was employed. The mesh resolution for both window areas and the CO_2 source area were set to 1 mm, and for building areas, it was set to 5 mm, while a coarser grid (50 mm) was chosen for areas further away. The expansion ratio between the two adjacent cells was kept below 1.2. To optimize computational efficiency and reduce processing time, the tetrahedral mesh in the fluid domain was transformed into polyhedral mesh within ANSYS Fluent. To ensure the accuracy of the numerical model, a mesh sensitivity analysis was conducted to assess the results' variation across different mesh sizes. The uncertainty arising from discretization was evaluated using the grid convergence index (GCI) method, which was introduced by Ref. [48]. The specifics and parameters of the analysis are provided below.

The calculation, first need to define the grid size *h*, ΔV_i is the volume, *N* is the total number of cells used for the computations.

$$h = \left[\frac{1}{N}\sum_{i=1}^{N}(\Delta V_i)\right]^{1/3} \quad (2)$$

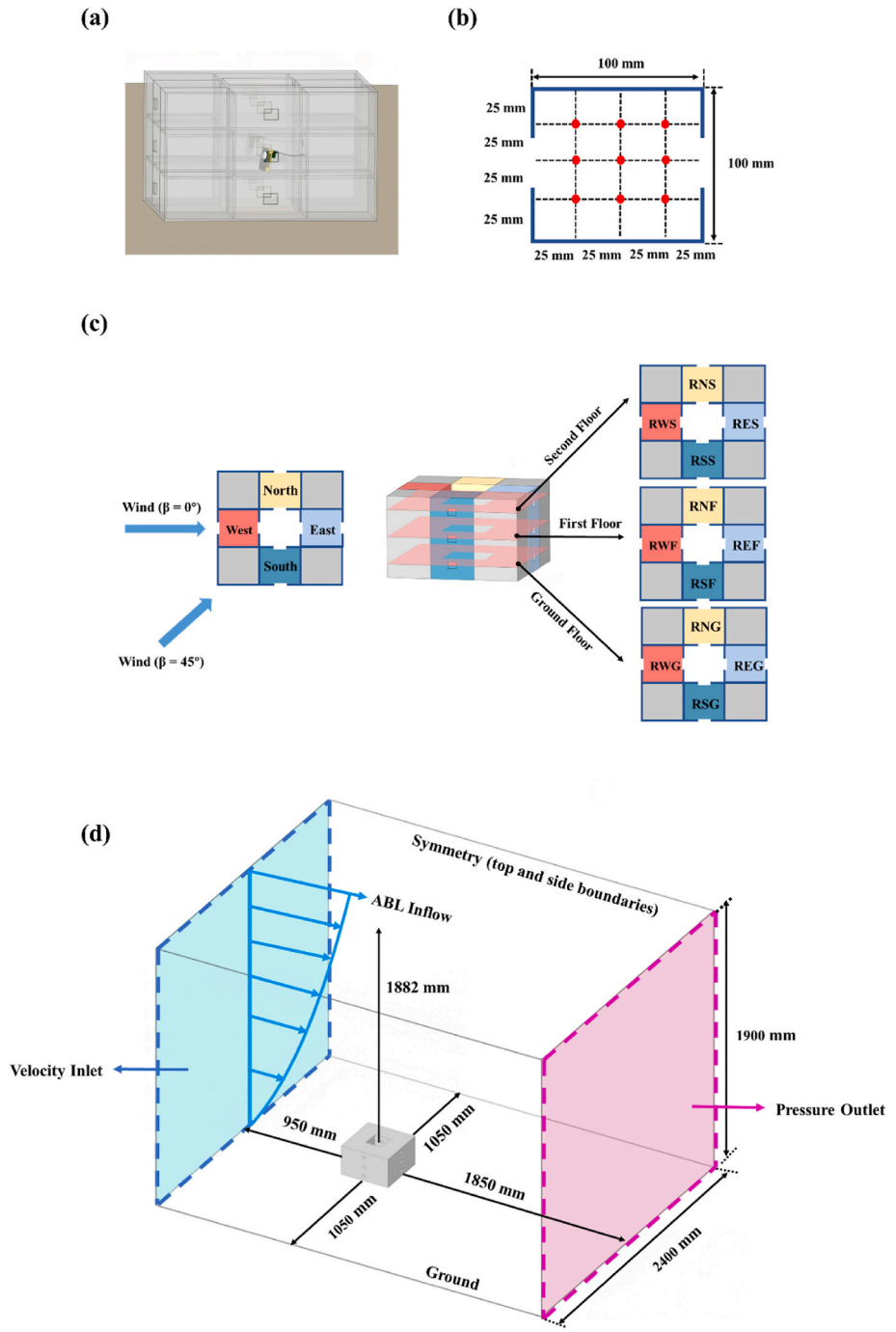

Fig. 5. (a) The courtyard building model for the CFD modeling. (b) Distribution of nine monitoring points inside the test room. (c) Orientation and naming of each test room for analysis. (d) The dimensions and boundary conditions of the computational domain.

As shown in Fig. 6 and Table 1, three distinct grid sizes—fine, medium, and coarse—were selected. Simulations were conducted to ascertain the values of pivotal variables (ϕ_1, ϕ_2, ϕ_3) pertinent to the study's objective. It is recommended that the grid refinement factor, denoted as [48]$r = h_{\text{coarse}}/h_{\text{fine}}$ exceeds 1.3 [48]. Given the conditions $h_1 < h_2 < h_3$, the ratios are defined as $r_{21} = h_2/h_1$, $r_{32} = h_3/h_2$. Consequently, the grid sizes were N1 (927,280), N2 (396,713), and N3 (178,630), resulting in r values of 1.327 and 1.305. The method's apparent order, p, can be derived using expressions from Eq. (3) to Eq. (5), where $\varepsilon_{32} = \phi_3 - \phi_2$, $\varepsilon_{21} = \phi_2 - \phi_1$.

$$p^* = \frac{1}{\ln(r_{21})}\left|\ln\left|\varepsilon_{32}/\varepsilon_{21}\right| + q(p^*)\right| \tag{3}$$

$$q(p^*) = \ln\left(\frac{r_{21}^{p^*} - s}{r_{32}^{p^*} - s}\right) \tag{4}$$

$$s = 1 \cdot \text{sgn}\left(\varepsilon_{32}/\varepsilon_{21}\right) \tag{5}$$

The extrapolated values based on Eq. (6):

$$\phi_{\text{ext}}^{21} = \left(r_{21}^{p^*}\phi_1 - \phi_2\right)/\left(r_{21}^{p^*} - 1\right) \tag{6}$$

The approximate relative error, denoted as e_a^{21}, the extrapolated relative error, e_{ext}^{21}, the extrapolated relative error, $\text{GCI}_{\text{fine}}^{21}$, can be determined using Eq. (7) to Eq. (9).

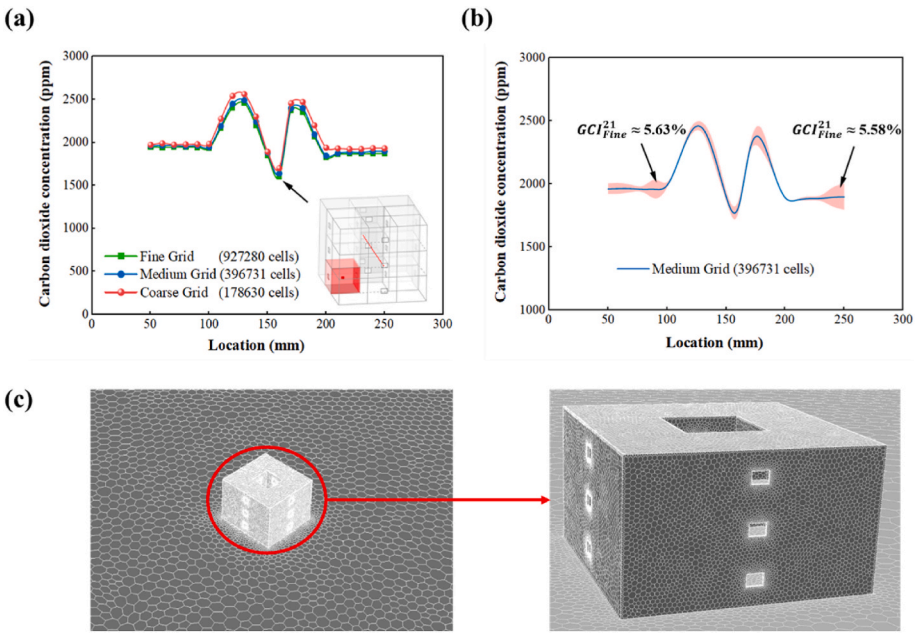

Fig. 6. (a) Simulated CO_2 concentration results along a horizontal centre line of the courtyard model at the height of 90 mm for the grid sensitivity analysis. (b) The grid sensitivity analysis was done using the GCI method. (c) The polyhedral mesh around the courtyard surfaces.

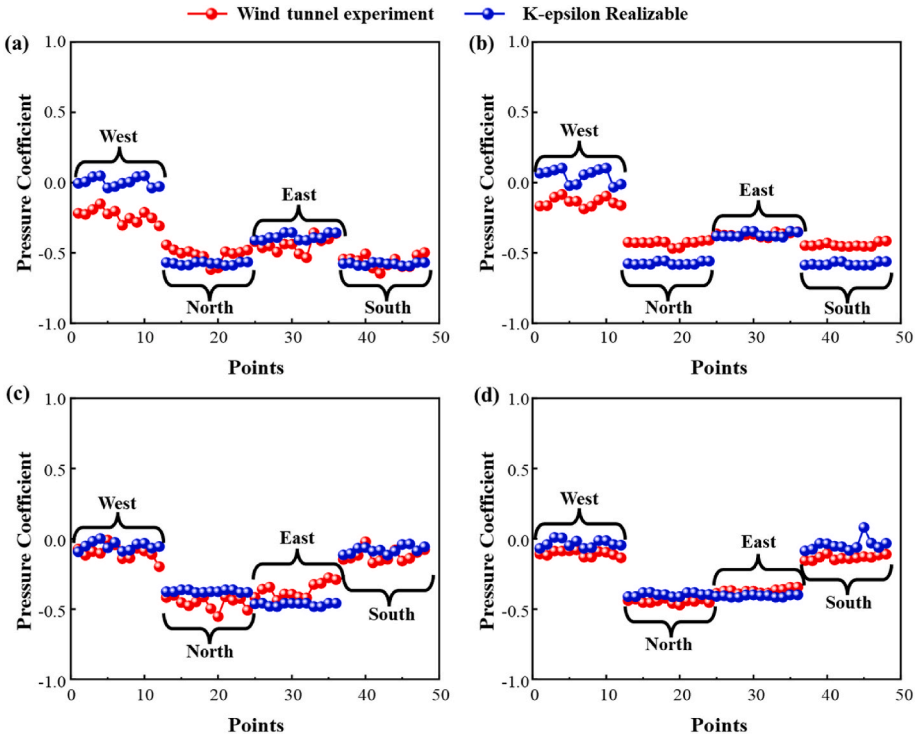

Fig. 7. Comparison of pressure coefficient values between the experiment and CFD simulations for (a) Wind direction at 0° and wind speed at U_{ref} = 4.51 m/s. (b) Wind direction at 0° and wind speed at U_{ref} = 8.86 m/s. (c) Wind direction at 45° and wind speed at U_{ref} = 4.51 m/s. (d) Wind direction at 45° and wind speed at U_{ref} = 8.86 m/s.

$$e_a^{21} = \left| \frac{\phi_1 - \phi_2}{\phi_1} \right| \tag{7}$$

$$e_{ext}^{21} = \left| \frac{\phi_{ext}^{12} - \phi_1}{\phi_{ext}^{12}} \right| \tag{8}$$

$$GCI_{fine}^{21} = \frac{1.25 e_a^{21}}{r_{21}^{p^*} - 1} \tag{9}$$

In this study, grid sensitivity was examined by selecting the first floor with coordinates X = 150 mm, Z = 90 mm, and Y ranging from 50 mm to 250 mm. A total of 21 points were chosen to observe the CO_2 concentration (ppm) under three different grid sizes, as depicted in Fig. 6 (a).

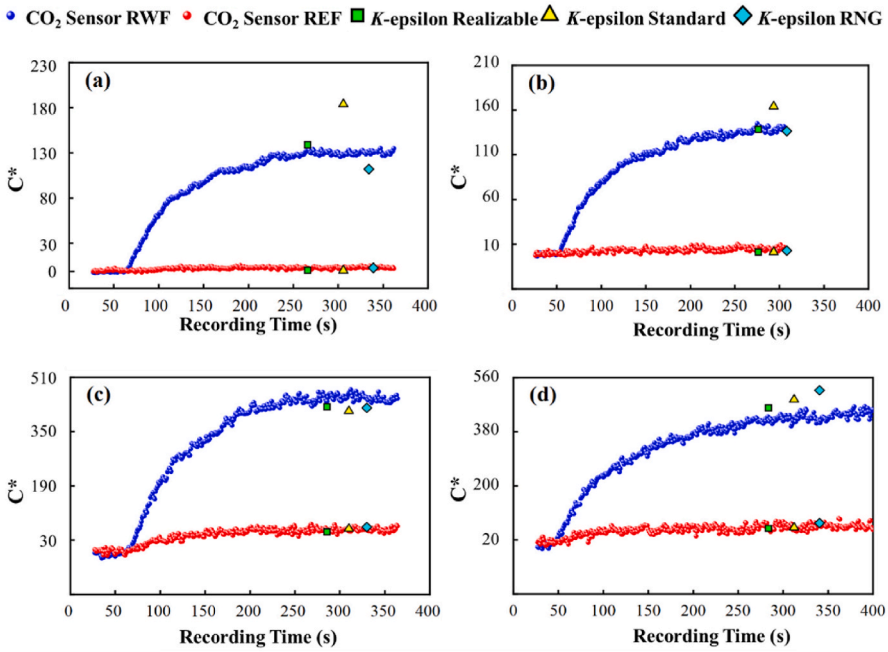

Fig. 8. Comparison of CO_2 dimensionless concentration C^* between the experiment and CFD simulations with three turbulence models, for (a) Wind direction at 0° and wind speed at U_{ref} = 4.51 m/s. (b) Wind direction at 0° and wind speed at U_{ref} = 8.86 m/s. (c) Wind direction at 45° and wind speed at U_{ref} = 4.51 m/s. (d) Wind direction at 45° and wind speed at U_{ref} = 8.86 m/s.

Table 1
Sample discretization error calculation using GCI method.

	CO_2 Concentration (ppm) at Y = 60 mm	CO_2 Concentration (ppm) at Y = 120 mm	CO_2 Concentration (ppm) at Y = 180 mm
N1	927,280	927,280	927,280
N2	396,713	396,713	396,713
N3	178,630	178,630	178,630
r_{21}	1.327	1.327	1.327
r_{32}	1.305	1.305	1.305
ϕ_1	1945.207	2405.236	2348.362
ϕ_2	1964.026	2448.301	2399.195
ϕ_3	1990.212	2540.542	2469.876
p^*	1.433	3.014	1.430
ϕ_{ext}^{21}	1907.567	2737.260	2246.481
e_a^{21}	0.967 %	1.790 %	2.165 %
e_{ext}^{21}	1.973 %	1.347 %	4.535 %
GCI_{fine}^{21}	2.419 %	1.662 %	5.423 %

Data presented in Table 1 specifically highlights Y = 60 mm, Y = 120 mm, and Y = 180 mm. The grid convergence index for these points is 2.419 %, 1.662 %, and 5.423 %, respectively. The medium mesh size was ultimately selected for this study, as its results exhibited minimal error compared to the fine mesh size, and computational cost savings were observed. Fig. 6 (b) illustrates the medium grid convergence index and discretization error bars for all 21 points, with the maximum GCI_{fine}^{21} being 5.63 %, and the average GCI_{fine}^{21} across the 21 points, being 2.210 %. Hence, the medium mesh size is well-suited for subsequent simulations.

3.4. Validation of the numerical model

This section compares wind tunnel experimental data with CFD simulations, focusing on two key areas: the internal surface pressure distribution and CO_2 dispersion in courtyard buildings. This comparison is crucial for verifying the precision and reliability of the computational models used.

3.4.1. Validation of internal room pressure distribution

The outcomes of the wind tunnel test and CFD simulations have been evaluated with a focus on the internal surface pressure coefficient (C_p), as defined by Eq. (10). In this context, ' P' denotes the observed pressure, while ' P_{ref}' and ' U_{ref}' represent the reference pressure and velocity, respectively. Additionally, ' ρ' signifies the air density.

$$C_p = \frac{P - P_{ref}}{0.5\rho U_{ref}^2} \tag{10}$$

In the wind tunnel experiments, the MPS4264 Scanivalve digital pressure transducer was employed to gather data on the pressure coefficient (C_p) at 48 monitoring points located inside courtyard buildings. This data was then compared against the results from CFD simulations. As indicated in Table 2, the study utilized two different wind speeds (U_{ref} = 4.51 m/s and U_{ref} = 8.86 m/s) and two wind directions (β = 0 and β = 45). Five commonly used RANS models were selected for this research: *k*-epsilon standard, *k*-epsilon RNG, *k*-epsilon Realizable, *k*-Omega standard, and *k*-Omega SST. Three validation metrics were applied: the normalized mean squared error (NMSE), the fractional bias (FB), and the fraction of predictions within a factor of two of the observations (FAC2). These metrics were employed to conduct a comprehensive and quantitative evaluation of the performance of all five RANS turbulence models, using Eq. (11) to Eq. (13).

$$FB = \frac{[O] - [P]}{0.5([O] + [P])} \tag{11}$$

$$\mathrm{NMSE} = \frac{\left[(O_i - P_i)^2\right]}{[O_i][P_i]} \tag{12}$$

$$\mathrm{FAC2} = \frac{1}{N}\sum_{i=1}^{N} n_i \text{ with } n_i = \begin{Bmatrix} 1 \text{ for } 0.5 \le \dfrac{P_i}{O_i} \le 2 \\ 0 \text{ else} \end{Bmatrix} \tag{13}$$

According to the results presented in Table 2, the RANS models demonstrate effective predictive capabilities for the flow characteristics around buildings, particularly in accounting for the influence of wind

Table 2
Validation metrics for the internal surface pressure coefficient.

Model		NMSE	FB	FAC2
Wind direction β = 0, Wind velocity = 4.51 m/s	*k*-epsilon standard	1.543	0.305	0.75
	k-epsilon RNG	1.529	0.099	0.750
	k-epsilon Realizable	1.031	0.130	0.750
	k-omega standard	1.573	0.073	0.750
	k-omega SST	1.946	0.135	0.750
Wind direction β = 0, Wind velocity = 8.86 m/s	*k*-epsilon standard	1.008	0.111	0.750
	k-epsilon RNG	1.766	−0.009	0.750
	k-epsilon Realizable	1.255	−0.063	0.750
	k-omega standard	2.074	−0.138	0.750
	k-omega SST	1.774	−0.035	0.750
Wind direction β = 45, Wind velocity = 4.51 m/s	*k*-epsilon standard	0.280	0.002	0.854
	k-epsilon RNG	0.358	0.260	0.521
	k-epsilon Realizable	0.292	0.068	0.813
	k-omega standard	0.643	0.242	0.542
	k-omega SST	0.351	0.153	0.542
Wind direction β = 45, Wind velocity = 8.86 m/s	*k*-epsilon standard	0.256	0.049	0.875
	k-epsilon RNG	0.413	0.274	0.500
	k-epsilon Realizable	0.218	0.177	0.625
	k-omega standard	0.796	0.414	0.500
	k-omega SST	0.519	0.321	0.500
Target, Acceptance criteria		0, <1.5	0, [-0.3, 0.3]	1, >0.3

direction and speed on wind pressure distribution. The performance of various turbulence models varies with wind directions at 0 and 45°. Under 0-degree wind direction, the *k*-epsilon Realizable model exhibits lower NMSE values (1.031 and 1.255 for wind speeds of U_{ref} = 4.51 m/s and U_{ref} = 8.86 m/s, respectively), acceptable FB values (0.13 and −0.063 respectively), and satisfactory FAC2 values (both 0.75). This indicates its accuracy in capturing pressure variations on the upwind (west) and downwind (east) sides. In the case of a 45-degree wind direction, the *k*-epsilon Realizable model particularly stands out. At a wind speed of 4.51 m/s, it achieves an NMSE value of 0.292, an FB value of 0.068, and a FAC2 value of 0.813; at 8.86 m/s, these values are 0.218, 0.177, and 0.625 respectively, significantly outperforming other models like *k*-epsilon standard and *k*-Omega SST. These findings suggest that the RANS models, especially the *k*-epsilon Realizable model, are highly effective in predicting wind pressure distribution within courtyard buildings. They provide accurate predictions under various wind directions and speeds. Therefore, due to its good performance across all key evaluation metrics, the *k*-epsilon Realizable model has been chosen for subsequent CFD simulations.

Fig. 7 shows the distribution of pressure coefficients at various measurement points within the courtyard building, with experimental data (red dots) compared with the predictions from the *k*-epsilon Realizable model (blue dots). These points cover the building's east, west, north, and south rooms, under wind conditions of 0 and 45° and wind speeds of U_{ref} = 4.51 m/s and U_{ref} = 8.86 m/s. The comparison of the red and blue dots for each scenario allows an evaluation of the model's alignment with the experimental data. The *k*-epsilon Realizable model results generally follow the experimental data well, particularly in capturing the wind pressure trends on both upwind (e.g., west side at 0° wind direction) and downwind (e.g., east side at 0°) aspects. It also shows good predictive accuracy for crosswind conditions (e.g., north, and south sides at 45°). The discrepancies between wind tunnel data and CFD predictions, notably on the west building's upwind side at 0°, could be influenced by factors like local turbulence at internal test points near openings and the inherent differences in turbulence model approaches. These factors can impact the precision of pressure coefficient measurements and the accuracy of simulation results. The fixed boundary conditions in CFD simulations also play a role, as they represent an averaged state of flow under specific wind conditions, contrasting with the more variable and transient nature of actual wind fields. Despite these, the *k*-epsilon Realizable model proves effective in predicting the pressure coefficient in courtyard building interiors under varying wind conditions.

3.4.2. *Validation of CO_2 dispersion in the courtyard buildings*

In this study, CO_2 is used as the pollutant in wind tunnel testing to investigate the cross-transmission of pollutants in the courtyard building through crossflow natural ventilation. The choice of CO_2 is driven by its availability and cost-effectiveness, along with their suitable sensitivity range, which make them ideal for this study. Additionally, the safety profile of CO_2, particularly its non-toxic nature at concentrations under 5000 ppm [49], makes it a viable option for our controlled experimental studies. Although it doesn't mimic the heavier molecular weight of SF_6 or the reactivity of C_2H_4, CO_2's properties closely resemble those of many indoor pollutants [50,51], making it relevant for studying airflow in buildings [52–54]. Despite the limitations of not encompassing all pollutants' properties, this research will maintain methodological rigor through frequent calibration and multiple test runs, ensuring the reliability of findings.

The transmitted pollutant dimensionless concentration coefficient value C^* was normalized based on the source strength, reference height, and velocity, as specified in Eq. (14) for area-source emissions [46,55].

$$C^* = \frac{c \cdot u_{ref} \bullet L_{ref}^n}{Q \bullet L_{ref}^2} \tag{14}$$

Where c represents the tracer gas's mass concentration in kg/m^3, u_{ref} is the wind velocity at the reference height of the courtyard model, measured at 4.51 m/s and 8.86 m/s. L_{ref} is the reference height H, which is 0.18 m. The exponent n for the area source is 0 [46]. And Q is the emission mass flow in kg/s.

Fig. 8 Shows a comparison of the dimensionless CO_2 concentration C^* between wind tunnel experiments and those from CFD simulations. This figure illustrates the dynamic evolution of CO_2 concentration in two test rooms, REF and RWF, as recorded by sensors. The observation period encompasses the entire duration from the initial release of CO_2 to its eventual stabilization. In our CFD simulations using the RANS model, the symbols in Fig. 8 represent steady-state concentrations at specific points within our domain. These values reflect equilibrium conditions where system variables stabilize, mirroring the experimental measurements which were concluded once the CO_2 concentration in these rooms reached a stable state. In the wind tunnel experiments, the ambient background CO_2 concentration was approximately 400 ppm, which is equivalent to C^* being 0. Rather than subtracting this background level

from our measurements, we included it in the results to allow a direct comparison between the baseline CO_2 levels and the levels with the added tracer gas. This approach provides a clearer understanding of the impact of the tracer gas on overall CO_2 concentrations. The data derived from three distinct turbulence models—*k*-epsilon standard model, *k*-epsilon RNG model, and *k*-epsilon Realizable model—are evaluated against the experimental measurements. The simulation parameters were configured to match the wind tunnel experimental setup. In the RWF room, both a CO_2 release source and a sensor were installed, whereas the REF room was equipped with a similar sensor. The results for the courtyard model at 0° wind speeds of $U_{ref} = 4.51$ m/s and $U_{ref} = 8.86$ m/s are detailed in Fig. 8 (a) and 8 (b), respectively, while Fig. 8 (c) and 8 (d) present findings at 45°. As anticipated, the CO_2 concentration in the room reduces with increasing wind speed, demonstrating the capability of natural ventilation to remove pollutants from indoor spaces.

In terms of accuracy, while all turbulence models provided reliable predictions for the REF room, the *k*-epsilon Realizable model stood out for its precision in the RWF room. The *k*-epsilon standard model, despite slight deviations, remained largely accurate. However, the *k*-epsilon RNG model, especially at 45° and $U_{ref} = 8.86$ m/s, showed notable divergence, even though its other predictions were consistent. This aligns with previous research that often favored the *k*-epsilon Realizable model and *k*-epsilon RNG models for pollutant dispersion predictions. In these four tested scenarios, the *k*-epsilon Realizable model, the *k*-epsilon Standard model, and the *k*-epsilon RNG model demonstrated good accuracies of approximately 93.51 %, 88.99 %, and 92.27 %, respectively, in predicting CO_2 concentration within the two rooms of the experiment. Overall, the numerical model accurately simulated the CO_2 concentration within the courtyard building.

4. Results and discussion

In line with the wind tunnel experiments, CFD simulations were carried out to model pollutant dispersion from various rooms under different wind directions and speeds. The two column heights represent wind speeds of $U_{ref} = 4.51$ m/s and $U_{ref} = 8.86$ m/s. A total of 48 scenarios are presented, as shown in Fig. 9. Cases 1–24 correspond to a wind direction of 0°, while Cases 25–48 are set at 45°. It is worth noting that in all simulation scenarios, the release rate of CO_2 is maintained at 2.8 ml/s. Our findings provide valuable insights into pollutant dispersion patterns in courtyard buildings using an idealized model. This approach, while not encompassing all real-world complexities, highlights the importance of understanding airflow and pollutant dynamics. Future research should consider more detailed and realistic scenarios, including simultaneous pollutant-generating activities and the presence of surrounding buildings, to enhance the applicability of the results.

4.1. Airflow movement and pollutant dispersion at 0° wind direction

4.1.1. Air flow velocity and pressure distribution

Fig. 10 (a) illustrates the airflow patterns in the courtyard building based on the CFD predictions. The wind enters from the left inlet boundary, impacting the building's upwind side. Here, the airflow splits—part enters through the windows while the remainder either passes over the building or shears off, exiting through the pressure outlet on the right. Significant air recirculation occurs on the downwind side. These airflow dynamics show air moving from the west side rooms into the courtyard, then flowing into the rooms on the north and south sides, with east-facing rooms receiving air from the downwind direction. These patterns remain consistent at wind speeds of $U_{ref} = 4.51$ m/s and $U_{ref} = 8.86$ m/s and a wind direction of 0°.

Fig. 10 (b) to 10 (e) illustrate the distribution of velocity and pressure in the vertical and horizontal cross-sections. Fig. 10 (c) and 10 (e) specifically illustrate that rooms on the upwind side of the courtyard are subject to positive pressure, while rooms on the downwind and lateral sides experience negative pressure. Fig. 10 (b) displays jets of airflow moving either upwards or downwards from the upwind facade into the

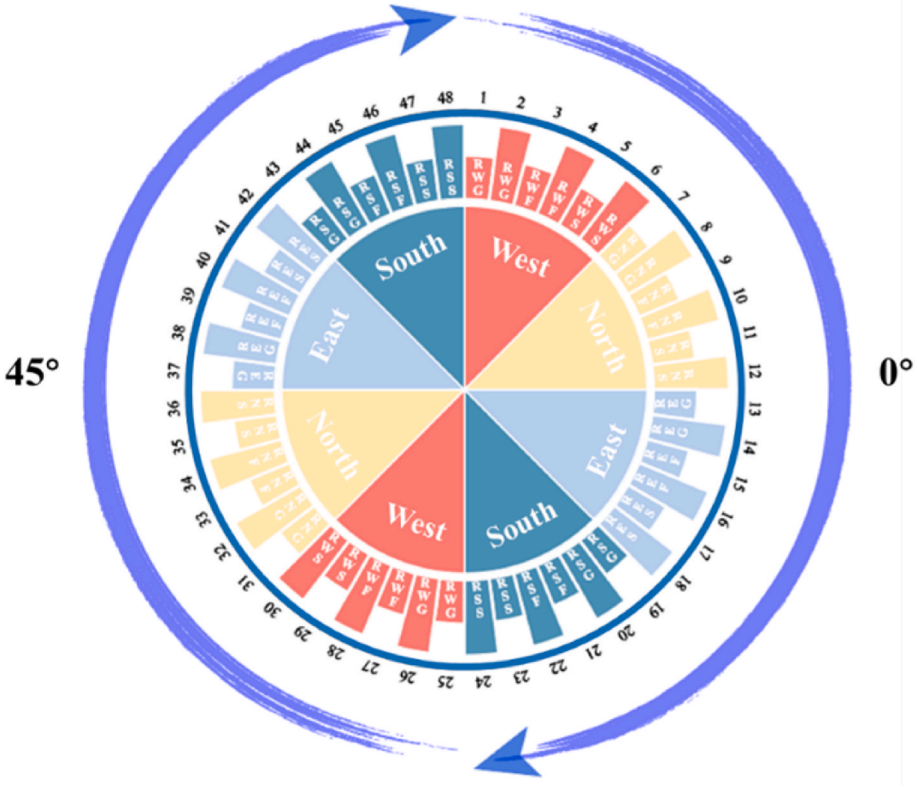

Fig. 9. 48 CFD simulation scenarios for evaluating the impact of different pollutant sources, wind speeds and directions.

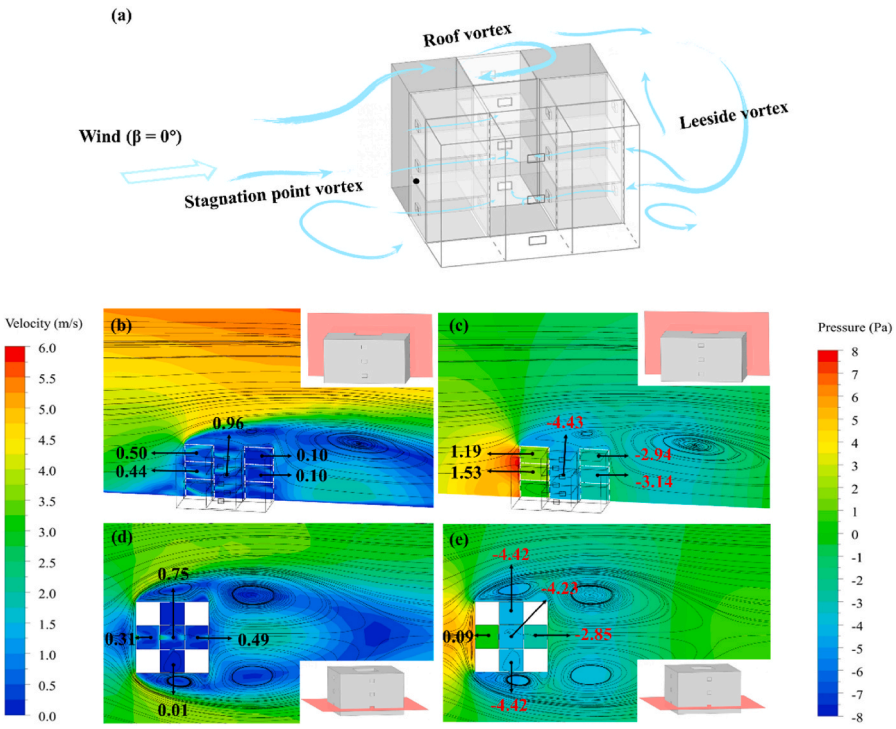

Fig. 10. (a) Observed airflow patterns in and around the courtyard building at 0° wind. (b) Cross-sectional contours of wind velocity distribution in vertical orientation around the courtyard building. (c) Pressure distribution in vertical orientation around the courtyard building. (d) Wind velocity in horizontal orientation around the courtyard building. (e) Pressure distribution in horizontal orientation around the courtyard building.

interior rooms, shaped by pressure differences. Additionally, smaller jets of airflow from the downwind rooms to the courtyard are observed, influenced by various pressure gradients.

Additionally, a portion of the incoming wind from the inlet, which does not enter the upwind rooms, generates a noticeable vortex on the downwind side as it traverses the courtyard. This vortex redirects a portion of the airflow back towards the courtyard on the downwind side. Fig. 10 (e) indicates a low-pressure zone in the courtyard, with the pressure dropping to an average of −4.23 Pa in the lower region. As observed in Fig. 10 (b) and 10 (d), the wind speed within the courtyard is higher (0.75 m/s on the lower region and 0.96 m/s on the upper region) compared to the adjacent rooms. Due to the lower pressure in the north and south (RN and RS) rooms, air from the courtyard is drawn towards these areas. The airflow speed in the ground-floor rooms of both RNG and RSG averages a modest 0.01 m/s, compared to the RWG and REG rooms where the wind speeds are notably higher at 0.31 m/s and 0.49 m/s, respectively.

4.1.2. CO_2 concentration and dispersion in the courtyard at 0° wind

Fig. 11 presents the predicted average concentrations of CO_2 in different rooms under two wind speeds and 0° wind direction, with a constant release rate of 2.8 m/l from different rooms or sources. It is evident that as wind speed increases, the rooms become more effective at expelling CO_2, but the observed trend remains similar under both wind speeds. When the source of pollution is located on either the upwind (west rooms) or downwind (east rooms) side rooms, in particular the ground and first floor, there is noticeable cross-transmission of CO_2 into the adjacent side rooms (RN and RS), aligning with the distribution of airflow in the courtyard as depicted in Fig. 10. For instance, at a wind speed of U_{ref} = 4.51 m/s, the highest concentration is observed in the north-facing room RNG (3211 ppm or C^* = 145.7) when pollutants are released from the downwind ground floor REG. The slower indoor wind speed leads to less effective CO_2 expulsion within the space. The second-highest concentration is found in the south-facing room RSG on the same floor, reaching 3100 ppm (C^* is 139.9). Furthermore, pollutants that diffuse from RWG and REG rooms on the ground floor to the courtyard also migrate to higher floors. As the distance increases between the source and the target room, the concentration of pollutants in the target rooms progressively decreases.

However, when the source of pollutants is from the side rooms (RN and RS), there is little to no increase in pollutant concentrations detected in any of the rooms. This aligns with the observed airflow patterns, which indicate that air flows from the courtyard into the side rooms and then exits outdoors. Consequently, the pollutants are effectively exhausted into the outdoor environment rather than in the courtyard. When the source of the pollutant is on the second floor, cross-transmission was mainly observed when the source was the upwind side room (RWS). This resulted in C^* of 28.1 and 34.4 being detected in adjacent side rooms on the same floor. Notably, the pollutants released from the second-floor rooms did not disperse to the lower floors. Additionally, when the source was the downwind side room (RES), the pollutant almost did not disperse towards the side rooms, unlike what was observed when the ground and first-floor rooms were the source. Pollutant concentrations are higher in some side rooms due to releases from the downwind room, influenced by the courtyard's airflow. The results indicate a downwash effect on the downwind side, where the airflow is deflected downward, causing pollutants to remain in the courtyard longer than those originating from the upwind rooms. This downward deflection traps pollutants in the courtyard, leading to higher concentrations and reduced dispersion compared to the airflow patterns from the upwind rooms. Comparing values in Fig. 11 with airflow patterns in Fig. 10 (b) reveals a clear difference: airflow from upwind rooms moves upward, while airflow from downwind rooms moves downward. This behavior corresponds with the observed pollutant distribution in the courtyard.

In Fig. 12 (a), the red lines indicate the pathway of CO_2 dispersion on the upwind side of the ground floor at a wind speed of U_{ref} = 4.51 m/s for Case 1. To better illustrate the dispersion pathway and the concentrations in the adjoining rooms, an enlarged view of the courtyard is presented in Fig. 12 (b), detailing the average CO_2 concentration in each

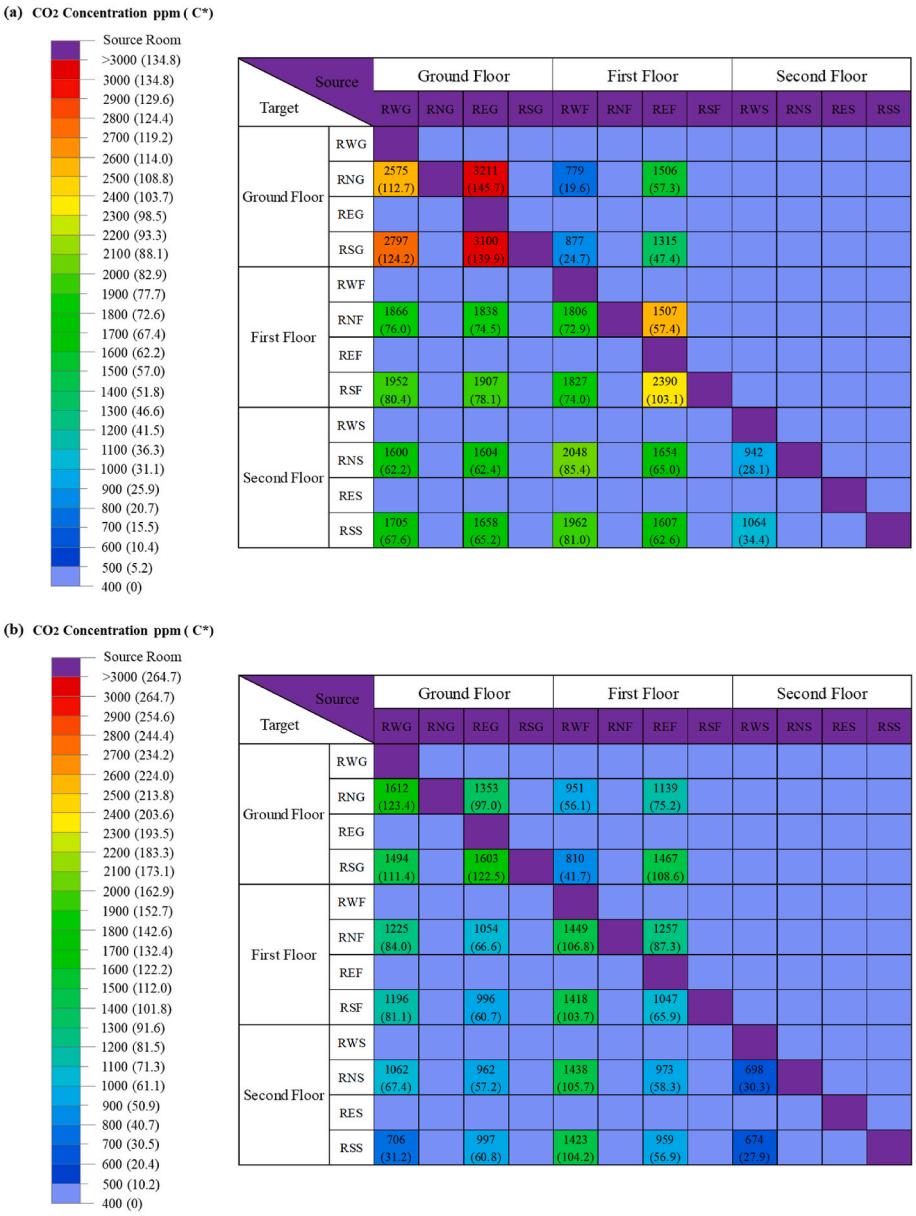

Fig. 11. Average concentrations of the CO_2 in different rooms at a wind speed of (a) U_{ref} = 4.51 m/s and (b) U_{ref} = 8.86 m/s, based on different source locations.

room. It is evident that when the source of pollution is on the upwind side, the primary pathway of dispersion is toward the immediately adjacent side rooms. Notably, there is no dispersion at the other two levels on the same upwind side and there is no dispersion into the rooms on the downwind side. As demonstrated in Fig. 12 (c) and 12 (d), the pathway of dispersion changes when pollutants originate from the downwind side of the ground floor under the same wind conditions. The pollutants diffuse into adjacent rooms on both sides and exist in the rooms on the downwind side of both the first and second floors with low levels.

4.2. Airflow movement and pollutant dispersion at 45° wind direction

4.2.1. Air flow velocity and pressure distribution

Fig. 13 (a) illustrates the observed airflow patterns around the courtyard when the wind approaches at a 45° wind angle. The results indicate that the incoming wind splits upon reaching the upwind sides of the courtyard. Some of the air enters the interior through the windows, while the remainder either passes over the top and sides of the courtyard and exits through the pressure outlet on the opposite side. The air that enters the rooms on the RW and RS (upwind) sides then flows into the central courtyard. Due to the pressure gradient, the air subsequently moves into the rooms on the downwind side (RE, RN), thus creating an "upwind-courtyard-downwind" flow system.

As shown in Fig. 13 (b), the velocity distribution reveals that the average wind speed is 0.59 m/s in the rooms on the upwind ground floor side, while it is 0.15 m/s and 0.86 m/s in the rooms on the downwind side. This is because when wind flows around a building, it can create complex airflow patterns, including vortices, on the downwind side. These vortices cause variations in wind speed and pressure distribution. As a result, different rooms on the downwind side experience different wind speeds depending on their position relative to the vortex. The average wind speed in the courtyard is 0.51 m/s Fig. 13 (c) shows the pattern of pressure distribution for the ground floor. In the upwind rooms, the pressure is positive, while it is negative in the downwind rooms, reaching −3.73 pa and −2.38 pa. In the courtyard, there is a low-pressure zone where the pressure is approximately −1.48 pa. This pressure gradient plays a major role in directing the airflow from the

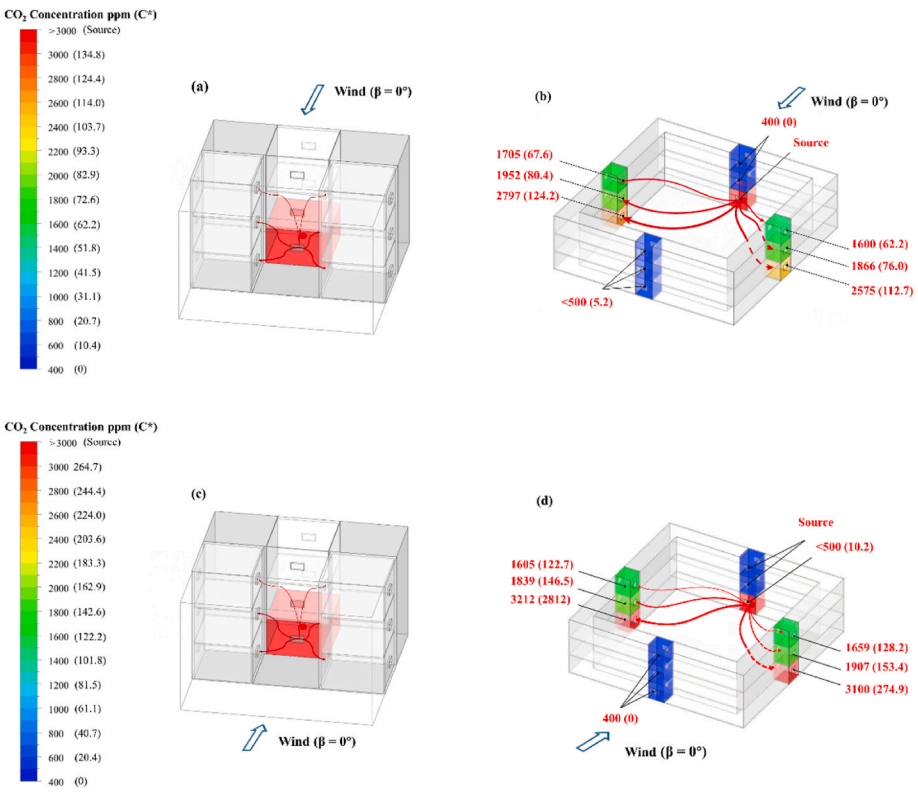

Fig. 12. Illustration of the CO_2 dispersion from the upwind side, showing the dispersion pathways and indoor concentration levels: (a) Dispersion pathways for Case 1. (b) Enlarged view of the dispersion pathways and indoor concentration levels for Case 1. (c) Dispersion pathways of Case 13. (d) Enlarged view of the dispersion pathways and indoor concentration levels for Case 13.

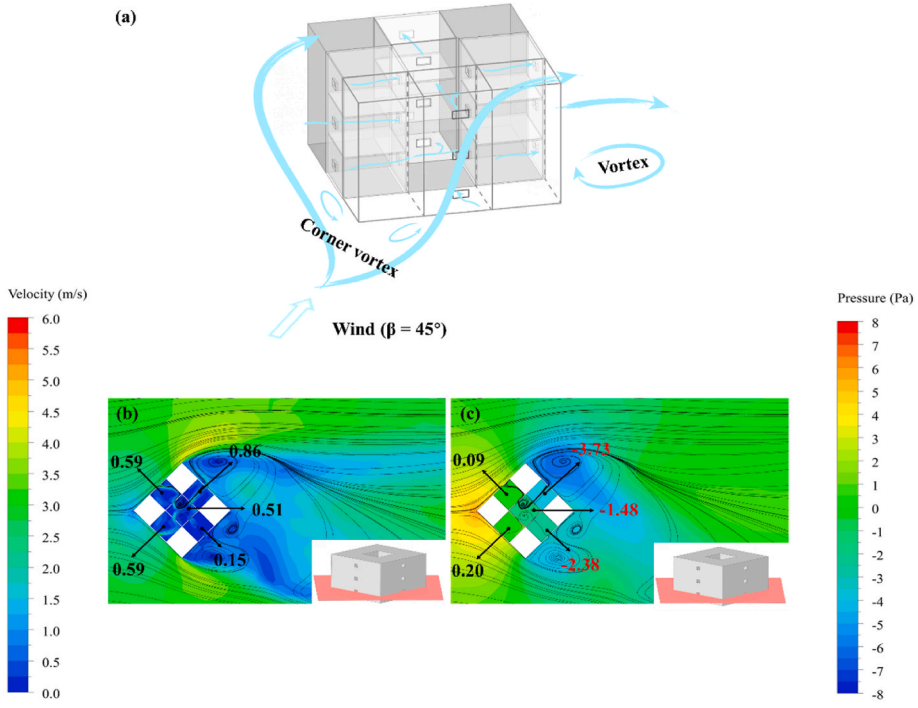

Fig. 13. (a) Observed airflow pattern in and around the courtyard building at 45° wind. (b) Cross-sectional contours of wind velocity distribution in horizontal orientation around the courtyard building. (c) Pressure distribution in horizontal orientation around the courtyard building.

courtyard towards the room RNG with a pressure of −3.73 pa. Conversely, the secondary airflow is directed to the room REG with a pressure of −2.38 pa.

4.2.2. CO_2 concentration and dispersion in the courtyard at 45° wind

Fig. 14 demonstrates the average concentrations of CO_2 in different rooms when the wind approaches the building at a 45-degree angle, with a release rate maintained at 2.8 ml/s. Comparing Fig. 14 (a) and 14 (b),

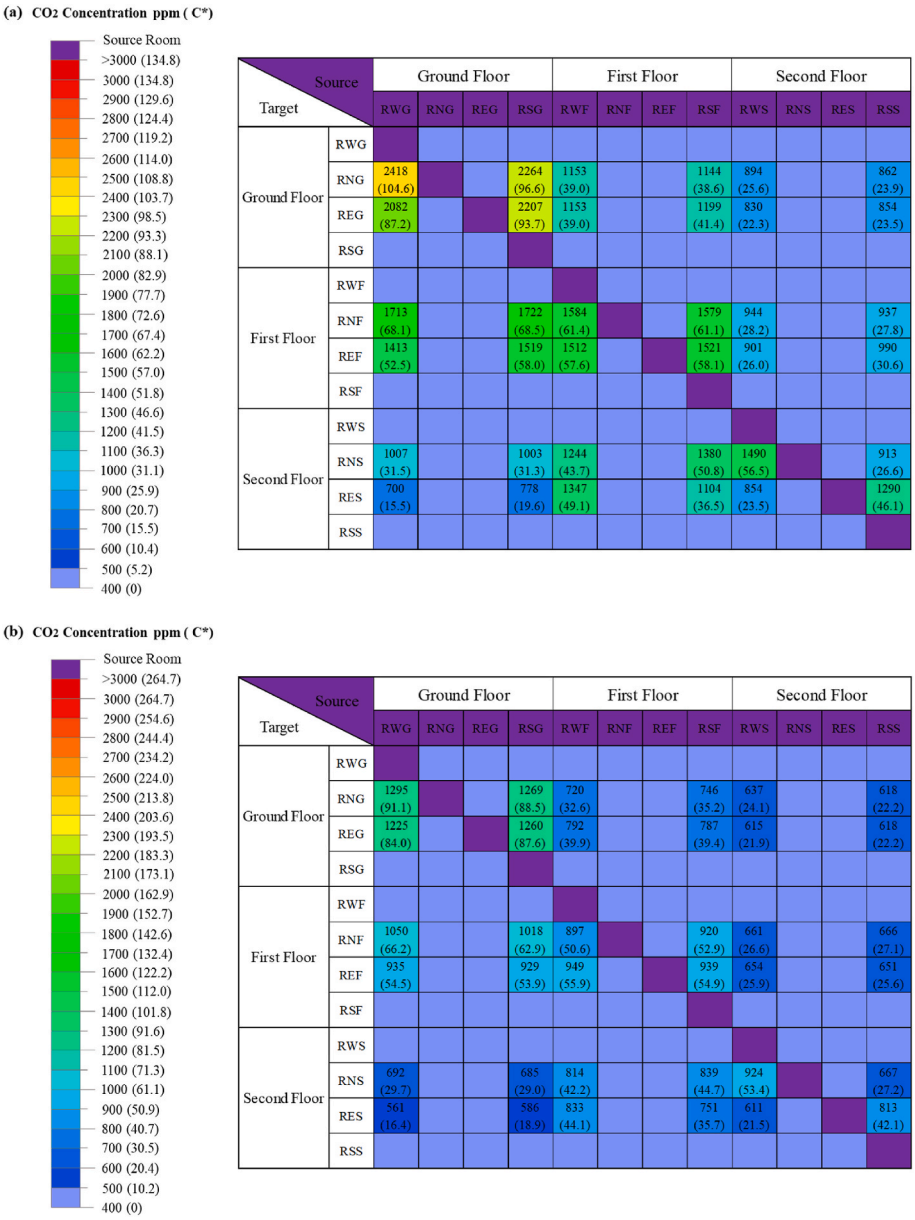

Fig. 14. Average concentrations of CO_2 in different rooms at a wind speed of (a) U_{ref} = 4.51 m/s and (b) U_{ref} = 8.86 m/s, based on different source locations.

which present the results for wind speeds of U_{ref} = 4.51 m/s and U_{ref} = 8.86 m/s respectively, it is evident that an increase in wind speed increase CO_2 expulsion within the rooms. It can be observed that the pollutants in the upwind rooms diffuse to the rooms on the downwind sides. For instance, when CO_2 is released in the RWG room upwind, it is detected only in the rooms on the downwind side. The concentration of CO_2 is higher on the same floor as its source, diminishing with elevation. Moreover, when the release source is in rooms at a greater elevation, there is a decreasing trend in CO_2 concentration, as shown by the peak concentration in any room. For example, at a wind speed of U_{ref} = 4.51 m/s, the concentration of CO_2 originating from the RSG room peaks at 2264 ppm in the RNG room, C^* increased more than 450 %. However, when the source of pollution is in the RSF and RSS rooms, the highest concentrations detected in the monitored rooms are 1579 ppm and 1290 ppm, respectively.

Fig. 15 (a) and Fig. 15 (b) depict the dispersion of CO_2 in the RWG room on the upwind side when the wind speed is U_{ref} = 4.51 m/s, denoted as Case 25. The right panel in the figure shows an enlarged view of the courtyard, detailing the pathway of dispersion and the level of concentrations in nearby rooms. Notably, when the source of pollution is on one of the upwind sides, the pollutants diffuse mainly into the two buildings on the downwind side, with no clear sign of dispersion into both upwind rooms. As the difference in pressure becomes more significant between the courtyard and the northern room, the airflow becomes faster in the north-facing room than in its east counterpart. In this case, there are more pollutants flowing from the courtyard to the northern room. Consequently, the indoor concentration of pollutants in the north-facing RNG room reaches 2418 ppm (C^* = 104.6), indicating a difference of approximately 330 ppm compared to the east-facing REG room.

As illustrated in Fig. 15 (c) and 15 (d), when the source of pollution is on the southern upwind side, the pollutants flow to the courtyard and then to the rooms on the downwind side. The concentration of pollutants remains higher in the north-facing room than in the east-facing room, maintaining the overall trend of dispersion. This is consistent with Case 43 when the wind speed is U_{ref} = 4.51 m/s. A similar trend has been observed at a wind speed of U_{ref} = 8.86 m/s.

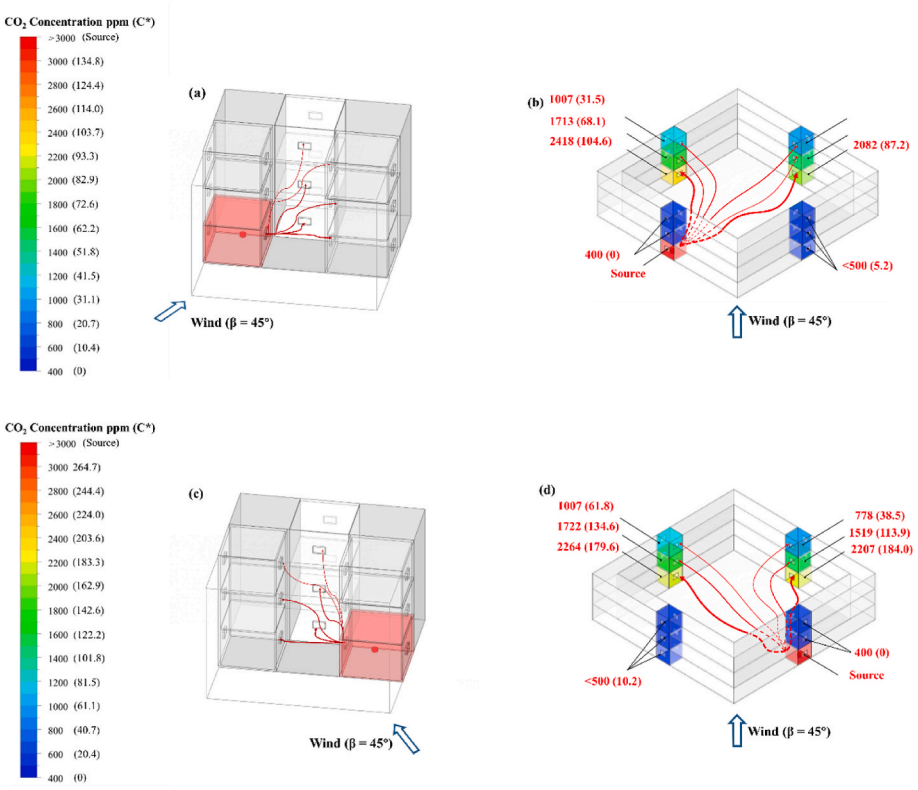

Fig. 15. Illustration of CO_2 dispersion from the upwind side, showing the dispersion pathways and indoor concentration levels: (a) Dispersion pathways for Case 25. (b) Enlarged view of the dispersion pathways and indoor concentration levels for Case 25. (c) Dispersion pathways of Case 43. (d) Enlarged view of the dispersion pathways and indoor concentration levels for Case 43.

5. Discussion

This section provides an analysis of the optimal and least favorable scenarios among the simulated 48 pollutant dispersion scenarios. Further identifying potential areas for improvement in this research. Our findings provide insights into pollutant dispersion patterns in courtyard buildings using an idealized model. This approach, while not including all real-world complexities, highlights the importance of understanding airflow and pollutant dynamics. The varying CO_2 emission rates established in our wind tunnel experiments, necessitated by the sensor's maximum detection limit, were carefully calibrated to ensure accurate readings without exceeding 5000 ppm. While this constraint led to different emission rates for 0° and 45° scenarios, the CFD model validation maintained consistent source values across all simulations. This methodology allowed us to explore a range of pollutant emission scenarios and understand their impact on dispersion patterns, albeit without directly comparing measurements between different wind angles due to differing initial conditions.

5.1. Comparative analysis of optimal and adverse scenarios

As shown in Fig. 16, at a wind direction of 0°, the dispersion of pollutants in the first 24 scenarios is analyzed at a wind speed of U_{ref} = 4.51 m/s and U_{ref} = 8.86 m/s. The most and least favorable conditions are then determined. At these wind speed, the optimal conditions for dispersion occur when the source of pollution is in the rooms facing north or south. Fig. 16 provides a detailed view of Cases 9, 10, 23, and 24. In these optimal scenarios, pollutants remain confined to the side rooms on all floors. This is attributed to the lower pressure in those rooms compared to the courtyard, which impedes the airflow from the courtyard into the side rooms where pollution originates. Thus, the dispersion of pollutants to other rooms is limited. Such confinement is considered optimal, as it minimizes the widespread dispersion of pollutants across multiple rooms. Conversely, in the least favorable scenarios, pollutants first diffuse from the source room to the courtyard and then to the other rooms, increasing the concentrations of CO_2.

Fig. 16 also illustrates four distinct scenarios at two different wind speeds. One scenario has the release source on the upwind side (Case 1 and Case 2), and the other has it on the downwind side (Case 13 and Case 14). It is evident that the pollutants disperse extensively into adjacent side rooms when the source of pollution is in the upwind and downwind rooms, especially to the rooms facing north or south on the same floor. Additionally, vertical dispersion into those rooms occurs, although it declines with height. At a wind speed of U_{ref} = 4.51 m/s and wind direction of 0°, the highest CO_2 concentrations are measured to be 3211 ppm (with the source on the downwind side in REG) and 2797 ppm (with the source on the upwind side in RWG). When the wind speed reaches U_{ref} = 8.86 m/s, CO_2 concentration exceeds 1600 ppm in some monitored rooms. Judging from Figs. 16 and 17, the optimal scenario is that the source of pollution is located in the rooms facing the north or the south, whereas the least favorable condition is that the source is in the rooms facing the east or the west, corresponding to the upwind or downwind side, respectively.

As shown in Fig. 17, at a wind direction of 45°, the patterns of dispersion of pollutants are evaluated at two different wind speeds across 24 different scenarios: U_{ref} = 4.51 m/s and U_{ref} = 8.86 m/s. According to the results, the best and the worst conditions for the dispersion of pollutants are identified. When the wind speed is U_{ref} = 4.51 m/s or U_{ref} = 8.86 m/s, the most favorable dispersion is observed when the pollutants originate from the rooms located on the north or east, indicating the downwind side in relation to the wind direction. In these scenarios, the pollutants tend to be trapped within the rooms on the downwind side without extensive dispersion to the courtyard or adjacent rooms. This is due to the lower pressure in the downwind rooms relative to the courtyard. Such a scenario is deemed optimal as it limits the dispersion of pollutants across different rooms.

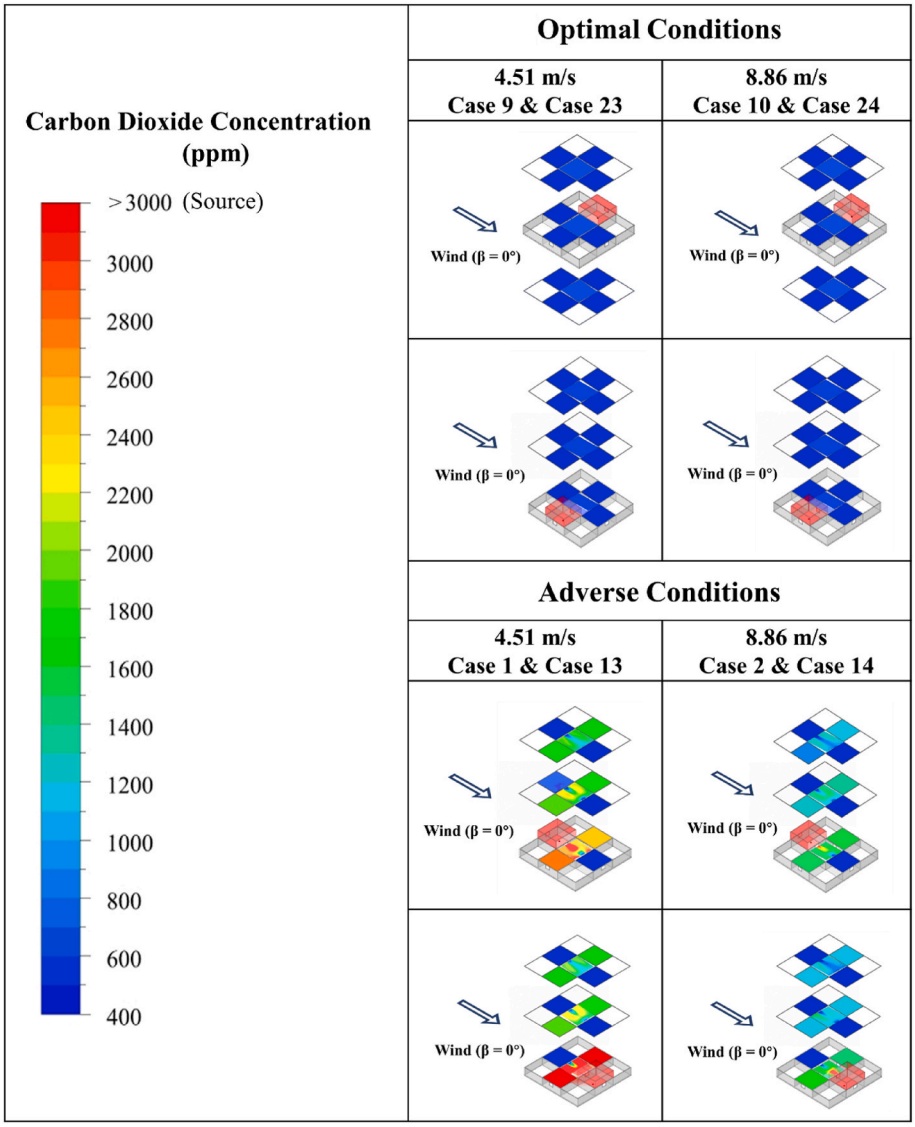

Fig. 16. Comparative analysis of optimal and adverse conditions across the first 24 scenarios under a wind speed of U_{ref} = 4.51 m/s and 8.86 m/s and wind direction of 0°.

In contrast, the least favorable dispersion occurs when pollutants diffuse into the courtyard and then spread to other rooms, increasing the concentration of CO_2. This is evident in Fig. 17 when the release source is in the upwind rooms or in the rooms directly facing the wind (Cases 25, 26, 43 and 44). The trend indicates a more pronounced dispersion of pollutants into the courtyard and subsequently into the downwind rooms, with higher CO_2 concentrations on the same floor as the source, diminishing with elevation. At a wind speed of U_{ref} = 4.51 m/s, the peak CO_2 concentrations reach 2418 ppm and 2264 ppm when the source of pollution is on the upwind side, respectively. At a wind speed of U_{ref} = 8.86 m/s, the concentrations exceed 1200 ppm in some rooms.

5.2. Limitations and recommendations for future works

This study is based on an idealized model designed to investigate pollutant dispersion in courtyard buildings, and while it provides foundational insights, it does not encompass all real-world complexities, such as simultaneous indoor pollutant-generating activities and the influence of surrounding structures. Firstly, one limitation of this study is the need to vary CO_2 release rates based on wind angles and speeds to avoid exceeding the sensor's maximum detection limit. Future research could address this by using sensors with higher detection limits or by employing additional methods to normalize emission rates across different scenarios. Additionally, further studies should consider more complex pollutant generation scenarios, including simultaneous activities and full-scale model analyses, to better reflect real-world conditions and enhance the applicability of the findings to practical architectural design. It should be noted that this study focuses on the dispersion of pollutants within courtyard architecture and solely considers cross ventilation as the ventilation strategy. However, there are significant differences in the wind environment of courtyards under single-sided ventilation compared to cross ventilation, which this paper does not explore.

Additionally, in this study, the size of window openings was set uniformly, without considering the potential impact of their variation on pollutant dispersion. For future research directions, exploring pollutant dispersion in courtyard architecture under single-sided ventilation conditions, as well as examining the impact of different opening sizes and orientations on pollutant dispersion, will be of significant value. This will not only provide more comprehensive guidance for ventilation strategies in courtyard architecture but also contribute to a deeper understanding of the impact of architectural design on indoor air quality.

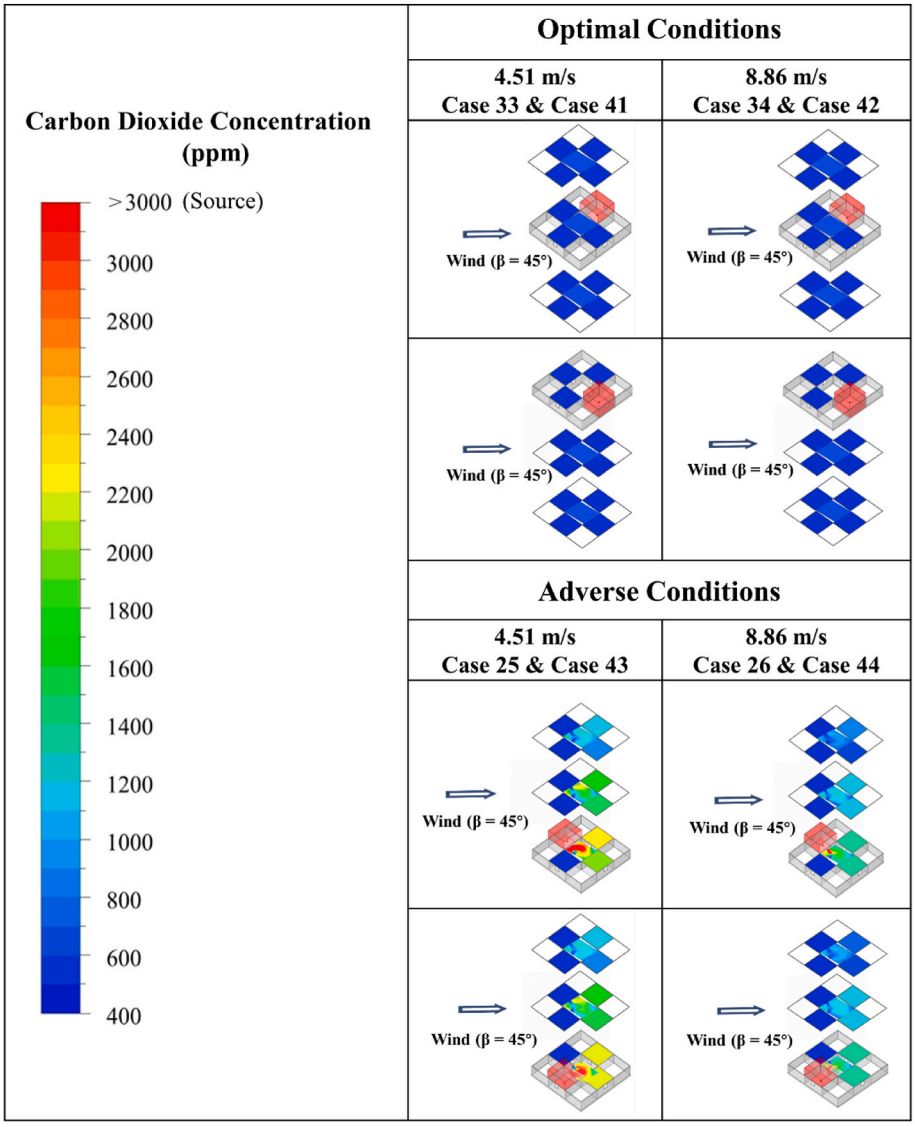

Fig. 17. Comparative analysis of optimal and adverse conditions across the following 24 scenarios under a wind direction of 45°.

Furthermore, while this study mainly focuses on the exploration of pollutant concentrations and dispersion paths, future research on factors such as air change rate in different rooms will also be extremely valuable, further promoting understanding and innovation in controlling and improving air quality within courtyard buildings.

For the validation and simulation of CFD, we selected the commonly used RANS models for comparison and application. RANS models are chosen for their ability to successfully predict airflow movement and pollutant dispersion in courtyard architecture, as well as their relatively lower computational cost. In this study, the *k*-epsilon Realizable model was selected based on the validation of wind tunnel experiments. Nevertheless, the study did not adopt LES models, based on considerations of computational resources and time efficiency. However, LES models are established for their high-accuracy simulation of complex flows, making them an important direction for future research. Therefore, in future work, comparing the differences and advantages of RANS and LES models in predicting pollutant dispersion in courtyard architecture will be an important research area. This will not only help us gain a deeper understanding of the applicability and accuracy of different models in specific architectural environments but also promote the development of more efficient and precise methods for simulating pollutant dispersion, providing stronger scientific support for courtyard architecture design.

6. Conclusion

This work conducts an in-depth investigation of the characteristics of pollutant dispersion in a crossflow ventilated courtyard architecture, employing a systematic approach that integrates wind tunnel experiments and CFD simulations. Unlike previous studies, this research, provides a detailed analysis of the dynamic process by which pollutants are transferred from indoors to outdoors and then recirculated back into other indoor areas through natural ventilation, thereby addressing a research gap in this field.

Through wind tunnel experiments, this study conducted assessment of the wind environment within courtyard buildings, particularly assessing indoor pressure distribution by measuring the surface pressure coefficient (C_p). Additionally, CO_2 concentrations in the source room and target rooms were monitored using CO_2 sensors. Two different wind speeds ($U_{ref} = 4.51$ m/s and $U_{ref} = 8.86$ m/s) and directions (0° and 45°) were selected for the experiments. The results of the CFD simulations were validated using wind tunnel experiments, comparing three different RANS models. The *k*-epsilon Realizable model was ultimately chosen as the turbulence model for subsequent research based on the

validation results. In the CFD model, 48 different scenarios of pollutant dispersion were set up with varying wind speeds and directions to analyze the dispersion effects when pollutants are placed in different rooms. The study found that:

(1) Cross-ventilation in courtyard buildings significantly affects the indoor-outdoor dispersion and re-entrance of pollutants, with wind direction having a notable impact on indoor pollutant concentrations. When the pollutant source is on the second floor, cross-transmission to other rooms is significantly lower than sources on the ground or first floor, regardless of the wind direction. This indicates a higher risk of pollutant spread and elevated indoor concentrations when sources are located on lower floors, highlighting the importance of effective ventilation strategies to mitigate these risks. Additionally, there is no significant transmission to vertically adjacent rooms or to rooms on the same side as the source, highlighting a pattern where pollutant dispersion is heavily influenced by the source's vertical and horizontal proximity.

For instance, when the pollutant source is located in a room on the west side of the ground floor (RWG) with a wind direction of 0°, pollutants will disperse to adjacent side rooms (RN and RS), usually not dispersing to the upper rooms on the same side (RWF and RWS) as the source, nor reaching the directly opposite or east side rooms. At a wind speed of $U_{ref} = 4.51$ m/s and wind direction of 0°, the highest CO_2 concentrations are measured to be 3211 ppm (with the source on the downwind side in REG) and 2797 ppm (with the source on the upwind side in RWG). When the wind direction is at 45°, a significant portion of the pollutants from the upwind rooms disperses to the opposing downwind rooms. Specifically, the CO_2 concentrations in the downwind ground-floor increase from a baseline of 400 ppm–2418 ppm and 2082 ppm, when the pollutant source is the upwind room RWG.

(2) The location of pollutant sources critically influences the dispersion patterns of contaminants. Under certain conditions, indoor pollutants may accumulate within specific rooms rather than dispersing to adjacent areas. For instance, at a wind direction of 0°, when pollutants originate from the north or south sides of a building, it has been observed that pollutants predominantly remain confined to the room of release. They seldom spread to other areas; the CO_2 concentrations in rooms other than the source typically stay close to the baseline level of approximately 400 ppm.

(3) Variations in wind speed significantly influence indoor pollutant concentrations, where higher wind speeds reducing the accumulation of pollutants and lower speeds leading to greater accumulation. However, changes in wind speed do not alter the direction of pollutant dispersion. For example, when the pollutant source is located in the RWG room, and the wind direction is at 0°, an increase in wind speed from $U_{ref} = 4.51$ m/s to $U_{ref} = 8.86$ m/s results in a decrease in CO_2 concentration in the RSG room from 2797 ppm to 1494 ppm. This observation highlights the critical role of wind speed in controlling indoor air quality and suggests that ventilation strategies should consider the modulation of airflow to effectively manage pollutant levels indoors.

(4) The circulation of pollutants, driven by natural ventilation from indoor spaces to courtyards and back indoors, significantly impacts rooms on the same floor as the source. This effect diminishes both on higher and lower floors as the vertical distance from the source increases. For instance, when the pollutant source is located on the ground floor's upwind side, and the wind enters at a 45° angle, the CO_2 concentration on the ground floor rooms on the downwind side increases up to 1682 ppm from a baseline of 400 ppm. In contrast, the first and second-floor rooms on the same side experience lower increases in pollutant concentrations of 1013 ppm and300 ppm, respectively.

This study, through the combination of wind tunnel experiments and CFD modeling, has revealed the patterns of pollutant dispersion in courtyard architecture and identified the optimal scenarios where pollutants do not disperse to the courtyard and surrounding rooms, as well as the worst scenarios where pollutants extensively disperse to other rooms through natural ventilation. These findings not only deepen the understanding of natural ventilation patterns in courtyard architecture and the resultant pollutant dispersion but also provide valuable guidance to architects and building designers aiming to create safer and more comfortable living environments.

Disclosure statement

No potential conflict of interest is reported by the authors.

CRediT authorship contribution statement

Hao Sun: Writing – review & editing, Writing – original draft, Visualization, Validation, Software, Resources, Methodology, Investigation, Formal analysis, Data curation, Conceptualization. **John S. Owen:** Writing – review & editing, Writing – original draft, Visualization, Validation, Supervision, Software, Project administration, Methodology, Investigation, Formal analysis, Data curation, Conceptualization, Writing – review & editing, Validation, Supervision, Resources, Investigation, Formal analysis, Data curation, Conceptualization. **Salah Almazmumi:** Validation, Methodology, Investigation, Data curation, Conceptualization. **Chong Liu:** Writing – review & editing, Visualization, Validation, Methodology, Investigation, Formal analysis, Data curation. **Murtaza Mohammadi:** Writing – review & editing, Validation, Methodology, Investigation. **Abdullah Dik:** Writing – original draft, Validation, Resources, Investigation, Formal analysis. **Carlos Jimenez-Bescos:** Supervision. **John Kaiser Calautit:** Writing – review & editing, Validation, Supervision, Project administration, Methodology, Investigation, Formal analysis, Conceptualization.

Declaration of competing interest

The authors declare that they have no known competing financial interests or personal relationships that could have appeared to influence the work reported in this paper.

Data availability

Data will be made available on request.

Acknowledgement

The authors would like to thank the support of the Department of Civil Engineering and the Department of Architecture and Built Environment of the University of Nottingham for providing the facility for carrying out the wind tunnel experiment, modeling and simulations.

Nomenclature

Abbreviation

ABL	Atmospheric Boundary Layer
CFD	Computational Fluid Dynamics
CO_2	Carbon dioxide
FAC2	Factor of Two
FB	Fractional Bias
FVM	Finite Volume Method
GCI	Grid Convergence Index
LES	Large Eddy Simulation
NMSE	Normalized Mean Squared Error
RANS	Reynolds-Averaged Navier-Stokes
RE	Rooms on the eastern side
REF	Room - Eastern - First Floor
REG	Room - Eastern - Ground Floor
RES	Room - Eastern - Second Floor
RN	Rooms on the northern side
RNF	Room - Northern - First Floor
RNG	Room - Northern - Ground Floor
RNS	Room - Northern - Second Floor
RS	Rooms on the southern side
RSF	Room - Southern - First Floor
RSG	Room - Southern - Ground Floor
RSS	Room - Southern - Second Floor
RW	Rooms on the western side
RWF	Room - Western - First Floor
RWG	Room - Western - Ground Floor
RWS	Room - Western - Second Floor

Symbols

α	Power law exponent
β	Wind direction (°)
C*	Dimensionless concentration coefficient
c	The mass concentration of the tracer gas (kg/m^3)
C_p	The pressure coefficient
h	Grid size
L	Reference hight (m)
N	Total number of grid cells
n	Exponent number
O	Observed value
P	Predicted value
p	Pressure (Pa)
p^*	The apparent order
r	The grid refinement factor
ρ	Density (kg/m^3)
S_{ct}	Schmidt number
u	Velocity (m/s)
V	Volume (m^3)
ϕ	The values of pivotal variable

Subscript

Coarse	Refers to variables with the coarse mesh size
ext	Extrapolated value
Fine	Refers to variables with the fine mesh size
i	Index for summation, ranging from 1 to N
Medium	Refers to variables with the medium mesh size
mv	Measured value
ref	Reference

Appendix

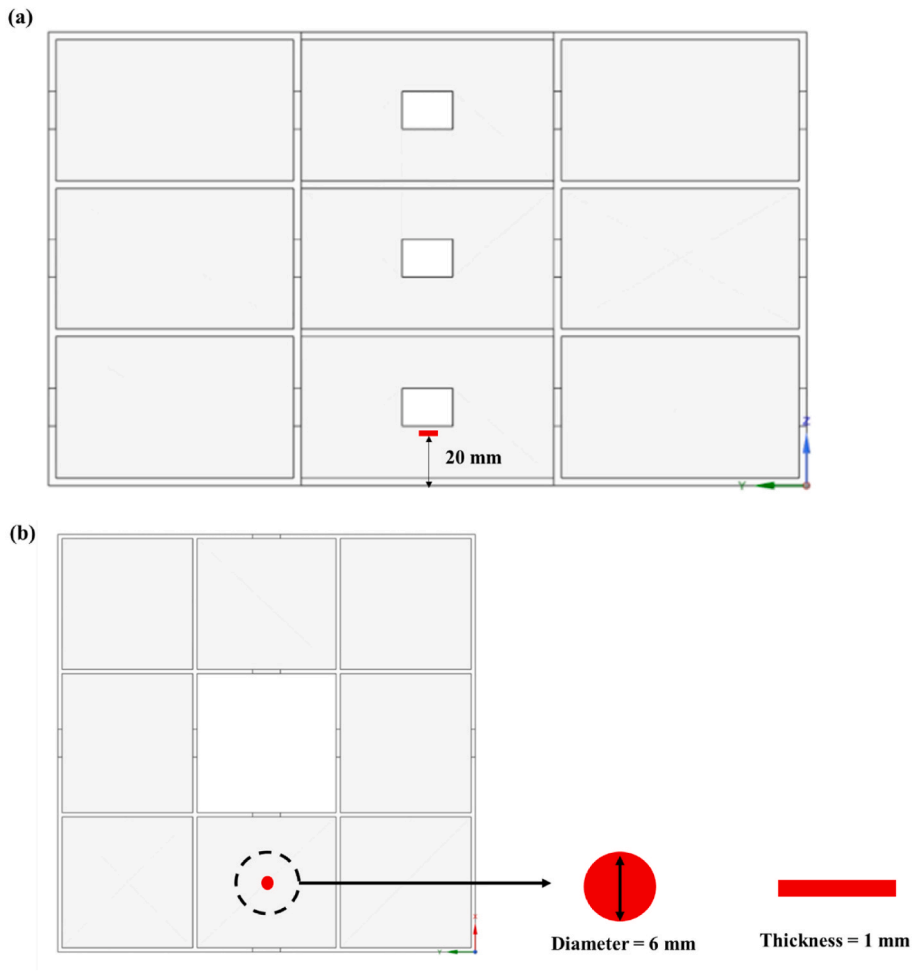

Fig. A.1. Configuration of CO_2 emission source in CFD simulations. (a) The vertical positioning of the CO_2 release source within the test room layout. (b) The horizontal positioning and dimensions of the emission source and its cylindrical geometry.

References

[1] H.W. Zheng, A Review of "Courtyard housing and cultural sustainability: theory, practice and product", By Donia Zhang, International Journal of Housing Policy 15 (2015) 509–511, https://doi.org/10.1080/14616718.2015.1092794.
[2] S. Gunasagaran, B.T. Shiowee, T. Mari, S. Srirangam, V.F.P. Ng, Revisiting the courtyard as lived heritage and social space, J. Eng. Sci. Technol. 17 (2022) 74–89.
[3] H. Sun, H. Zhong, A. Dik, K. Ding, C. Jimenez-Bescos, J.K. Calautit, Numerical investigation of evaporative cooling strategies on the aero-thermal performance of courtyard buildings in hot-dry climates, Build. Environ. 258 (2024) 111588, https://doi.org/10.1016/j.buildenv.2024.111588.
[4] J. Leng, Q. Wang, K. Liu, Sustainable design of courtyard environment: from the perspectives of airborne diseases control and human health, Sustain. Cities Soc. 62 (2020) 102405, https://doi.org/10.1016/j.scs.2020.102405.
[5] S. Sharples, R. Bensalem, Airflow in courtyard and atrium buildings in the urban environment: a wind tunnel study, Sol. Energy 70 (2001) 237–244, https://doi.org/10.1016/S0038-092X(00)00092-X.
[6] I. Rajapaksha, H. Nagai, M. Okumiya, A ventilated courtyard as a passive cooling strategy in the warm humid tropics, Renew. Energy 28 (2003) 1755–1778, https://doi.org/10.1016/S0960-1481(03)00012-0.
[7] Z. Zamani, S. Heidari, P. Hanachi, Reviewing the thermal and microclimatic function of courtyards, Renew. Sustain. Energy Rev. 93 (2018) 580–595, https://doi.org/10.1016/j.rser.2018.05.055.
[8] M. Li, Y. Jin, J. Guo, Dynamic characteristics and adaptive design methods of enclosed courtyard: a case study of a single-story courtyard dwelling in China, Build. Environ. 223 (2022) 109445, https://doi.org/10.1016/j.buildenv.2022.109445.
[9] E. Jamei, P. Rajagopalan, M. Seyedmahmoudian, Y. Jamei, Review on the impact of urban geometry and pedestrian level greening on outdoor thermal comfort, Renew. Sustain. Energy Rev. 54 (2016) 1002–1017, https://doi.org/10.1016/j.rser.2015.10.104.
[10] E. Andreou, Thermal comfort in outdoor spaces and urban canyon microclimate, Renew. Energy 55 (2013) 182–188, https://doi.org/10.1016/j.renene.2012.12.040.
[11] E. Andreou, The effect of urban layout, street geometry and orientation on shading conditions in urban canyons in the Mediterranean, Renew. Energy 63 (2014) 587–596, https://doi.org/10.1016/j.renene.2013.09.051.
[12] M. Taleghani, M. Tenpierik, A. van den Dobbelsteen, Indoor thermal comfort in urban courtyard block dwellings in The Netherlands, Build. Environ. 82 (2014) 566–579, https://doi.org/10.1016/j.buildenv.2014.09.028.
[13] O. Al-Hafith, S. B K, S. Bradbury, P. de Wilde, The Impact of courtyard parameters on its shading level an experimental study in Baghdad, Iraq, Energy Proc. 134 (2017) 99–109, https://doi.org/10.1016/j.egypro.2017.09.539.
[14] X. He, W. Gao, R. Wang, Impact of urban morphology on the microclimate around elementary schools: a case study from Japan, Build. Environ. 206 (2021) 108383, https://doi.org/10.1016/j.buildenv.2021.108383.
[15] H. Sun, C. Jimenez-Bescos, M. Mohammadi, F. Zhong, J.K. Calautit, Numerical investigation of the influence of vegetation on the aero-thermal performance of buildings with courtyards in hot climates, Energies 14 (2021) 5388, https://doi.org/10.3390/en14175388.
[16] J. Zhu, J. Feng, J. Lu, Y. Chen, W. Li, P. Lian, X. Zhao, A review of the influence of courtyard geometry and orientation on microclimate, Build. Environ. 236 (2023) 110269, https://doi.org/10.1016/j.buildenv.2023.110269.
[17] F. Trindade Da Silva, N.C. Reis, J.M. Santos, E.V. Goulart, C. Engel De Alvarez, The impact of urban block typology on pollutant dispersion, J. Wind Eng. Ind. Aerod. 210 (2021) 104524, https://doi.org/10.1016/j.jweia.2021.104524.
[18] J. You, M. Wang, J. Li, S. Xu, C. Cao, S. Shao, Influence of cooking pollutant diffusion regularity by high-rise residential inner-courtyard forms in Wuhan, Buildings 12 (2022) 1452, https://doi.org/10.3390/buildings12091452.

[19] V. Lozhkin, O. Lozhkina, V. Dobromirov, A study of air pollution by exhaust gases from cars in well courtyards of Saint Petersburg, Transport. Res. Procedia 36 (2018) 453–458, https://doi.org/10.1016/j.trpro.2018.12.124.
[20] Š. Nosek, Z. Kluková, M. Jakubcová, Z. Jaňour, The effect of courtyard buildings on the ventilation of street canyons: a wind-tunnel study, J. Wind Eng. Ind. Aerod. 220 (2022) 104885, https://doi.org/10.1016/j.jweia.2021.104885.
[21] P. Moonen, V. Dorer, J. Carmeliet, Evaluation of the ventilation potential of courtyards and urban street canyons using RANS and LES, J. Wind Eng. Ind. Aerod. 99 (2011) 414–423, https://doi.org/10.1016/j.jweia.2010.12.012.
[22] I.P. Castro, A.G. Robins, The flow around a surface-mounted cube in uniform and turbulent streams, J. Fluid Mech. 79 (1977) 307–335, https://doi.org/10.1017/S0022112077000172.
[23] B. Blocken, T. Stathopoulos, P. Saathoff, X. Wang, Numerical evaluation of pollutant dispersion in the built environment: comparisons between models and experiments, J. Wind Eng. Ind. Aerod. 96 (2008) 1817–1831, https://doi.org/10.1016/j.jweia.2008.02.049.
[24] Y. Tominaga, T. Stathopoulos, Numerical simulation of dispersion around an isolated cubic building: comparison of various types of k–ε models, Atmos. Environ. 43 (2009) 3200–3210, https://doi.org/10.1016/j.atmosenv.2009.03.038.
[25] Y. Tominaga, T. Stathopoulos, Numerical simulation of dispersion around an isolated cubic building: model evaluation of RANS and LES, Build. Environ. 45 (2010) 2231–2239, https://doi.org/10.1016/j.buildenv.2010.04.004.
[26] D. Guo, F. Yang, X. Shi, Y. Li, R. Yao, Numerical simulation and wind tunnel experiments on the effect of a cubic building on the flow and pollutant diffusion under stable stratification, Build. Environ. 205 (2021) 108222, https://doi.org/10.1016/j.buildenv.2021.108222.
[27] L.J. Hunter, G.T. Johnson, I.D. Watson, An investigation of three-dimensional characteristics of flow regimes within the urban canyon, Atmospheric Environment. Part B, Urban Atmosphere 26 (1992) 425–432, https://doi.org/10.1016/0957-1272(92)90049-X.
[28] N. Koutsourakis, J.G. Bartzis, N.C. Markatos, Evaluation of Reynolds stress, k-ε and RNG k-ε turbulence models in street canyon flows using various experimental datasets, Environ. Fluid Mech. 12 (2012) 379–403, https://doi.org/10.1007/s10652-012-9240-9.
[29] Y. Tominaga, T. Stathopoulos, CFD modeling of pollution dispersion in a street canyon: comparison between LES and RANS, J. Wind Eng. Ind. Aerod. 99 (2011) 340–348, https://doi.org/10.1016/j.jweia.2010.12.005.
[30] M. Lateb, C. Masson, T. Stathopoulos, C. Bédard, Numerical simulation of pollutant dispersion around a building complex, Build. Environ. 45 (2010) 1788–1798, https://doi.org/10.1016/j.buildenv.2010.02.006.
[31] M. Carpentieri, P. Hayden, A.G. Robins, Wind tunnel measurements of pollutant turbulent fluxes in urban intersections, Atmos. Environ. 46 (2012) 669–674, https://doi.org/10.1016/j.atmosenv.2011.09.083.
[32] P.-Y. Cui, Z. Li, W.-Q. Tao, Wind-tunnel measurements for thermal effects on the air flow and pollutant dispersion through different scale urban areas, Build. Environ. 97 (2016) 137–151, https://doi.org/10.1016/j.buildenv.2015.12.010.
[33] P.-Y. Cui, Y. Zhang, W.-Q. Chen, J.-H. Zhang, Y. Luo, Y.-D. Huang, Wind-tunnel studies on the characteristics of indoor/outdoor airflow and pollutant exchange in a building cluster, J. Wind Eng. Ind. Aerod. 214 (2021) 104645, https://doi.org/10.1016/j.jweia.2021.104645.
[34] F. Yang, Y. Kang, Y. Gao, K. Zhong, Numerical simulations of the effect of outdoor pollutants on indoor air quality of buildings next to a street canyon, Build. Environ. 87 (2015) 10–22, https://doi.org/10.1016/j.buildenv.2015.01.008.
[35] C.-R. Chu, K.-J. Yang, Transport process of outdoor particulate matter into naturally ventilated buildings, Build. Environ. 207 (2022) 108424, https://doi.org/10.1016/j.buildenv.2021.108424.
[36] Y. Tominaga, B. Blocken, Wind tunnel analysis of flow and dispersion in cross-ventilated isolated buildings: impact of opening positions, J. Wind Eng. Ind. Aerod. 155 (2016) 74–88, https://doi.org/10.1016/j.jweia.2016.05.007.
[37] X.P. Liu, J.L. Niu, K.C.S. Kwok, J.H. Wang, B.Z. Li, Investigation of indoor air pollutant dispersion and cross-contamination around a typical high-rise residential building: wind tunnel tests, Build. Environ. 45 (2010) 1769–1778, https://doi.org/10.1016/j.buildenv.2010.02.003.
[38] F. Bazdidi-Tehrani, S. Masoumi-Verki, P. Gholamalipour, Impact of opening shape on airflow and pollutant dispersion in a wind-driven cross-ventilated model building: Large eddy simulation, Sustain. Cities Soc. 61 (2020) 102196, https://doi.org/10.1016/j.scs.2020.102196.
[39] E. Mercker, A blockage correction for automotive testing in a wind tunnel with closed test section, J. Wind Eng. Ind. Aerod. 22 (1986) 149–167, https://doi.org/10.1016/0167-6105(86)90080-2.
[40] P.-Y. Cui, Z. Li, W.-Q. Tao, Investigation of Re -independence of turbulent flow and pollutant dispersion in urban street canyon using numerical wind tunnel (NWT) models, Int. J. Heat Mass Tran. 79 (2014) 176–188, https://doi.org/10.1016/j.ijheatmasstransfer.2014.07.096.
[41] P.-Y. Cui, W.-Q. Chen, J.-Q. Wang, J.-H. Zhang, Y.-D. Huang, W.-Q. Tao, Numerical studies on issues of Re-independence for indoor airflow and pollutant dispersion within an isolated building, Build. Simulat. 15 (2022) 1259–1276, https://doi.org/10.1007/s12273-021-0846-z.
[42] B.E. Launder, D.B. Spalding, The numerical computation of turbulent flows, Comput. Methods Appl. Mech. Eng. 3 (1974) 269–289, https://doi.org/10.1016/0045-7825(74)90029-2.
[43] V. Yakhot, S.A. Orszag, S. Thangam, T.B. Gatski, C. Speziale, Development of turbulence models for shear flows by a double expansion technique, Phys. Fluid. Fluid Dynam. 4 (1992) 1510–1520.
[44] T.-H. Shih, W.W. Liou, A. Shabbir, Z. Yang, J. Zhu, A new k-ϵ eddy viscosity model for high Reynolds number turbulent flows, Comput. Fluid 24 (1995) 227–238, https://doi.org/10.1016/0045-7930(94)00032-T.
[45] Y. Tominaga, T. Stathopoulos, Turbulent Schmidt numbers for CFD analysis with various types of flowfield, Atmos. Environ. 41 (2007) 8091–8099, https://doi.org/10.1016/j.atmosenv.2007.06.054.
[46] VDI 3783 Blatt 12 - environmental meteorology - physical modelling of flow and dispersion processes in the atmospheric boundary layer - application of wind tunnels, Engl. VDI/DIN-Kommission Reinhaltung der Luft (KRdL) - Normenausschuss (2000), in: https://www.vdi.de/en/home/vdi-standards/details/vdi-3783-blatt-12-environmental-meteorology-physical-modelling-of-flow-and-dispersion-processes-in-the-atmospheric-boundary-layer-application-of-wind-tunnels. (Accessed 2 July 2024).
[47] [online], Ansys Fluent Theory Guide 2021R2, Ansys Inc., 2021, https://www.ansys.com/. (Accessed 20 January 2023).
[48] P.J. Roache, Perspective: a method for uniform reporting of grid refinement studies, Journal of Fluids Engineering-Transactions of The Asme 116 (1994) 405–413.
[49] K. Azuma, N. Kagi, U. Yanagi, H. Osawa, Effects of low-level inhalation exposure to carbon dioxide in indoor environments: a short review on human health and psychomotor performance, Environ. Int. 121 (2018) 51–56, https://doi.org/10.1016/j.envint.2018.08.059.
[50] L.A. Graham, L. Noseworthy, D. Fugler, K. O'Leary, D. Karman, C. Grande, Contribution of vehicle emissions from an attached garage to residential indoor air pollution levels, J. Air Waste Manag. Assoc. 54 (2004) 563–584.
[51] X. Zhang, P. Wargocki, Z. Lian, Physiological responses during exposure to carbon dioxide and bioeffluents at levels typically occurring indoors, Indoor Air 27 (2017) 65–77.
[52] T. Bartzanas, C. Kittas, A.A. Sapounas, Ch Nikita-Martzopoulou, Analysis of airflow through experimental rural buildings: sensitivity to turbulence models, Biosyst. Eng. 97 (2007) 229–239, https://doi.org/10.1016/j.biosystemseng.2007.02.009.
[53] T. Van Hooff, B. Blocken, CFD evaluation of natural ventilation of indoor environments by the concentration decay method: CO2 gas dispersion from a semi-enclosed stadium, Build. Environ. 61 (2013) 1–17, https://doi.org/10.1016/j.buildenv.2012.11.021.
[54] W. Zhang, L. Wang, Z. Ji, L. Ma, Y. Hui, Test on ventilation rates of dormitories and offices in university by the CO2 tracer gas method, Procedia Eng. 121 (2015) 662–666, https://doi.org/10.1016/j.proeng.2015.08.1061.
[55] M. Mohammadi, J.K. Calautit, J.S. Owen, C. Gromke, Y. Wu, H. Liu, Inter-room pollutant transmission routes in naturally ventilated street canyon buildings, J. Build. Eng. 79 (2023) 107510, https://doi.org/10.1016/j.jobe.2023.107510.